Published OnlineFirst October 7, 2011; DOI:10.1158/0008-5472.CAN-11-2389



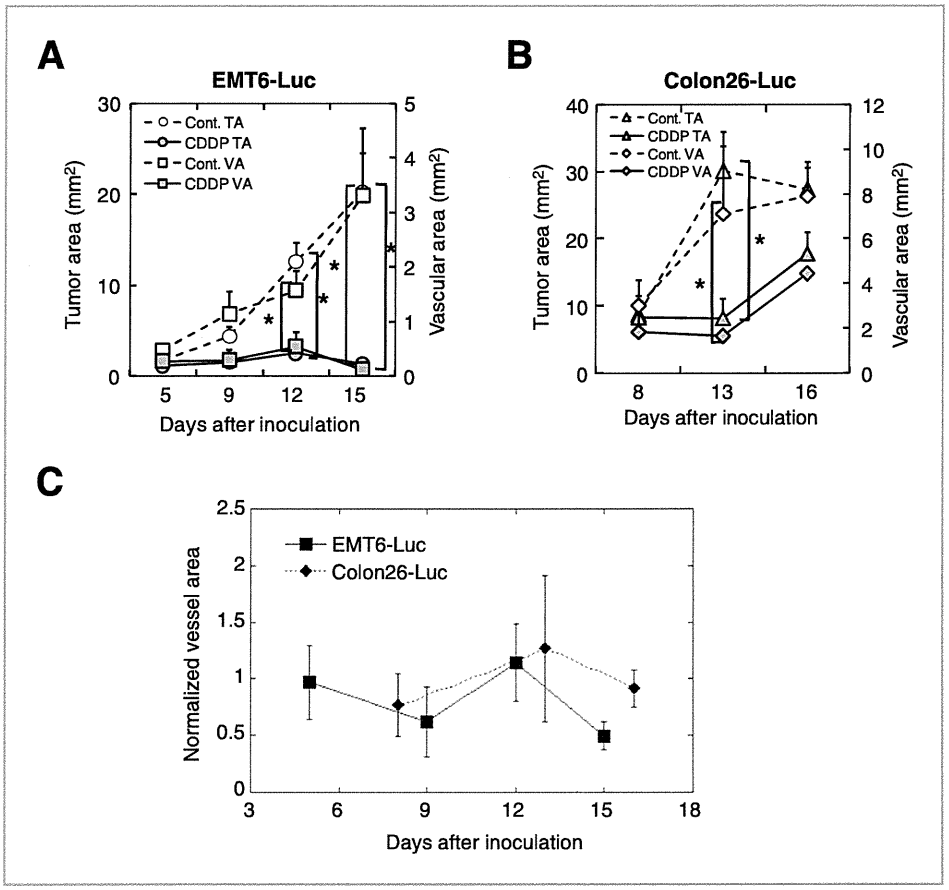


Figure 3. Quantification of intratumoral vessels with the combination of ALs, the HF-US imaging system, and the CDSD method. A, change of the tumor area (TA) and vessel area (VA) in EMT6-luc tumor: In the control groups, TA (open circle) and VA (open square) increased over 15 days. However, in the treatment group, TA (solid circle) and VA (solid square) were constant at lower levels over the same period. Significant differences in TA and VA between the control and treatment groups were found on days 12 and 15 (TA; $P < 0.05$, Student $t$ test, VA; $P < 0.05$, Student $t$ test). B, change of the tumor area (TA) and vessel area (VA) in Colon26-Luc tumor: In the control groups, TA (open triangle) and VA (open rhombus) increased until day 13 and thereafter saturated, whereas in the treatment group, the growth of TA (solid triangle) and VA (solid rhombus) was suppressed until day 13, then increased. Significant differences in TA and VA between the control and treatment groups were detected only on day 13 (TA; $P < 0.05$, Student $t$ test, VA; $P < 0.05$, Student $t$ test). *, $P < 0.05$. C, change of the normalized vessel area in the CDDP treatment group of the EMT6-Luc tumor (solid square) and of the Colon26-Luc tumor (solid rhombus). The normalized vessel area was given as (normalized vessel area) = [(CDDP VA)/(CDDP TA)]/[(Cont. VA)/(Cont. TA)]. In both tumors, there was no significant difference in the normalized vessel ratio over the experiment period (1-way ANOVA).

area (CDDP VA) were restricted with CDDP treatments, in which TA is the internal area that is defined by the circumference of the solid tumor in B-mode image and VA is the area occupied by vessel in the TA extracted by the CDSD method. Therefore, both TA and VA have unit. The extent of suppression in the EMT6-Luc tumor was larger than in the Colon26-Luc tumor. Significant differences between the control and treatment group for the EMT6-Luc tumors were observed on days 12 and 15 ($P < 0.05$, Student $t$ test), whereas they were detected on day 13 for Colon26-Luc tumors ($P < 0.05$, Student $t$ test). Figure 3C shows the relation between the normalized vessel area in the CDDP-treated tumor and the number of days after inoculation, in which (normalized vessel area) = [(CDDP VA)/(CDDP TA)]/[(Cont. VA)/(Cont. TA)]. For the EMT6-Luc tumors, the vessel ratio decreased slightly on days 9 and 15, but there was no significant difference over 15 days (1-way ANOVA). Similarly, the Colon26-Luc tumors show no significant difference over the same time period (1-way ANOVA). Although CDDP contributed to inhibition of tumor growth, these results indicate that the intratumoral vessel ratios in both tumors were constant; that is, the ratio is independent of the tumor size.

### Evaluation of the vessel ratio per inner or outer regions of the Colon26-Luc tumor, extracted from the 2D vascular image constructed using AL, the HF-US imaging system, the CDSD method, and immunohistochemical staining

Next, we investigated the change of the vessel ratio in the inner and outer regions of the Colon26-Luc tumor. Figure 4A shows an image that was binarized to enhance the vascular structure based on Fig. 2Bd. The tumor area was divided into inner and outer areas. Similarly, the immunohistochemical slides were divided into inner and outer areas. The endothelial-specific antigen CD31-positive cells in the inner and outer areas are shown in Fig. 4C and D, respectively.

Published OnlineFirst October 7, 2011; DOI:10.1158/0008-5472.CAN-11-2389



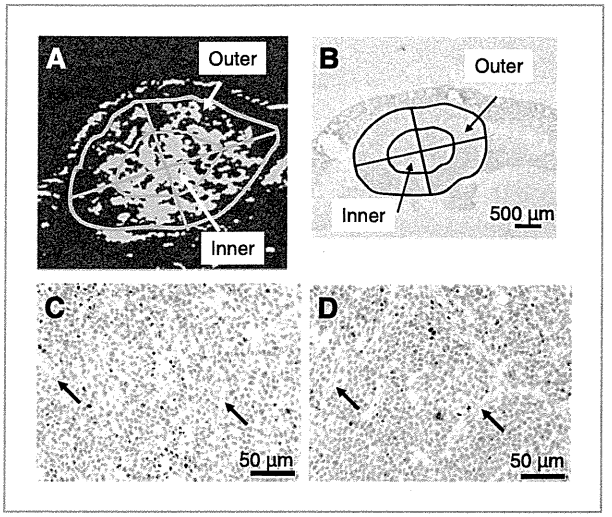


Figure 4. Vessel structure in the inner and outer regions of the Colon26-Luc tumor, extracted with the combination of ALs, the HF-US imaging system, and the CDSD method, and subsequent immunohistochemical analysis with CD31. A, reconstructed 2D vascular image. Both the inner and outer regions were divided into 4 sections each. B, CD31 immunostaining section, divided into inner and outer regions. Each region was divided into 4 subregions. The hotspot analysis was conducted for 8 subregions in total. C, positive staining for CD 31 (arrow) at tumor inner area. D, positive staining for CD31 (arrow) at tumor outer area.

Figure 5A shows the vascular ratio in the inner and outer regions with and without CDDP treatments on days 8, 13, and 16, obtained by 2D US images. The vessel ratios of the outer region were about double those of the inner region on all days in both the control and treatment groups. Figure 5B shows the vascular ratio obtained by immunohistochemical analysis. Similarly, the vessel ratio of the outer region was about double that of the inner region on all days, although the inner vessel ratios on day 13 were decreased compared with the ratios on day 8. The vascular ratio obtained by AL, the HF-US imaging system, and the CDSD method (Fig. 5A) was about 10 times higher than the ratio obtained by immunohistochemical analysis (Fig. 5B).

## Discussion

To our knowledge, this is the first article on the assessment of effects on tumor volume and angiogenesis by CDDP by using ALs, a HF-US system, and the CDSD method. Because the *in vivo* half-life of ALs with a mean diameter of 200 nm is less than 90 seconds (Fig. 2), enough amount of ALs may not leak out to the vascular space by the EPR effect within the short limited period time and thus ALs may not be used as pure EPR tracers. In case of mice bearing sarcoma 180 tumor, within 10 minutes radioiodinated *N*-(2-hydroxypropyl) methacrylamide copolymers of MW ranging from 4.5 k to 800 k were accumulated effectively in the tumor (17). Therefore, development of long-circulating liposomes with a life time more than at least 10 minutes may be desired to reveal the EPR effect (3). Previously, angiogenesis has been evaluated by US backscatter images

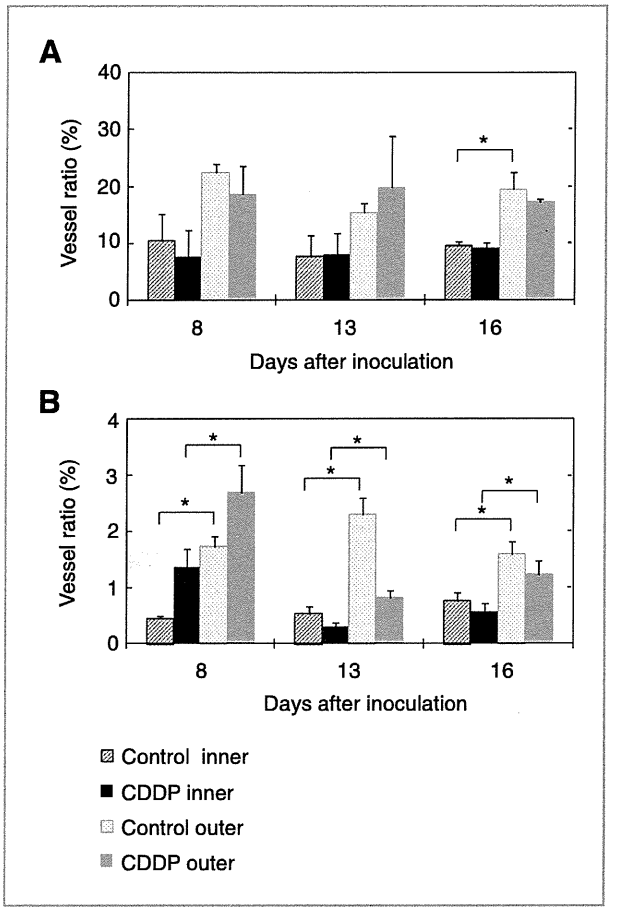


Figure 5. Comparison of vessel ratio of the Colon26-Luc tumor between the ultrasound constructed 2D vascular image and CD31 immunostaining. A, quantitative analysis of the vessel ratio based on ultrasound constructed 2D vascular image in the CDDP-treated and control tumors. B, quantitative analysis of the vessel ratio based on CD31 immunostaining. *, $P < 0.05$, Student $t$ test.

(18, 19). The simplest model of acoustic scattering from small particles is described by Rayleigh's model (20). When the particle diameter, $d$ is much smaller than the wavelength of the sound, the scattering cross section, $\sigma_S$ increases by frequency, $f$ to the 4th power, and by $d$ to the 6th power. However, Rayleigh's model is not suitable for calculating the scatter of sound from a single bubble because it ignores resonance. Following a scattering model based on a linear bubble equation, $\sigma_S$ increases by $f^4$ for frequencies well below resonance, whereas $\sigma_S$ is independent of the frequency, for frequency above resonance. For diameters smaller than the resonance diameter, $\sigma_S$ increases to the 6th power of the diameter, $\sigma_S \propto d^6$. For diameters larger than the resonance diameter, $\sigma_S \propto d^2$ (21, 22). Assuming that ALs are free bubbles and their mean diameter is 200 nm, the natural frequency was calculated to be 27 MHz (23). This frequency is on the same order as that used in the present experiment, that is, a central frequency of 40 MHz with an axial resolution of 40 μm. The calculated scattering cross section is 0.03 $\mu m^2$, which is emitted by a single bubble with a diameter of 200 nm. Because the bubble size is within the

Published OnlineFirst October 7, 2011; DOI:10.1158/0008-5472.CAN-11-2389



spatial resolution of the US system, the single bubble cannot be visualized. Thus, the intratumoral vascular images observed in the experiment might be the result of scattering of AL aggregation, ALs with larger sizes that cannot be eliminated from AL production process, or the oscillation of ALs at around 27 MHz.

The main function of CDDP is to damage DNA and induce apoptosis (24, 25). Although CDDP is not thought to inhibit angiogenesis specifically, some researchers have reported that CDDP provided antiangiogenic effects against several human and mouse cancer cells, including Colon26 carcinoma (26, 27). In addition, the larger vessels in the outer area of tumor are less affected by the antiangiogenic therapy, but small vessels perfused in the tumor are more sensitive to the therapy (1, 28, 29). It is believed that this effect depends on the accessibility of drugs to the endothelial cells in each vessel. In other words, most large vessels were stabilized by smooth muscle actin-positive cells, but immature small vessels in the tumor lacked coverage by smooth muscle cells and pericytes (29, 30). In the present experiment, both the tumor volume and the luciferase activities of murine mammary carcinoma EMT6-Luc tumor and murine colon carcinoma Colon26-Luc tumor were suppressed by about 1/10th and two-thirds of each control group by intratumoral injection of CDDP 3 times, respectively (Fig. 1). Because the vessel ratios of the inner and outer regions have similar values to those of the controls, CDDP may not inhibit angiogenesis specifically (Fig. 5). In the rapid growth phase of solid tumors, enhanced permeability of the neovascularity and limited lymphatic drainage was induced, resulting in the accumulation of fluid in the central tumor region, followed by an increase in the interstitial fluid pressure. The increased pressure constricts the vessels and decreases blood flow in the central regions (30, 31), leading to a decrease in the vessel ratio in the inner region rather than in the outer region (Fig. 5). The vessel ratio obtained by using ALs, the HF-US imaging system and the CDSD method (Fig. 5A) is 10 times higher than that of the value obtained by immunohistochemical analysis (Fig. 5B). The difference is caused by multiple factors: (a) the vessel area was expanded owing to the US scattering effect; and (b) the slice thickness resolution of the HF-US is 40 μm, whereas the thickness of the paraffin slides was 3 to 3.5 μm. Therefore, vascular information of US images should be 10 times more than the paraffin, and (c) the hotspot analysis was applied to an area of high vascular density within a tissue slide and not to the whole area of the slide (16). Therefore, vascular images obtained by ALs, the HF-US imaging system, and the CDSD method have ill-defined borders, which are not consistent with the vascular structures obtained by immunohistochemical analysis (32). Conventional noncontrast-enhanced Doppler US has been applied successfully to monitor antiangiogenic therapies; however, it is relatively insensitive to slow blood flow velocities and capillary blood flow in small nonstabilized vessels (28), which mostly respond to antiangiogenic treatments (33, 34). Recently, high-frequency volumetric power Doppler ultrasound (HF-VPDU; ref. 31) and contrast-enhanced HF-VPDU (1) have been investigated to assess antiangiogenic therapy effects. Ultrasound microbubble contrast agents that have been used in clinic are pure intravascular probes (35). They have the potential to target disease-related cellular and molecular process within the vascular compartment (35). Although ALs are one of several kinds of UCAs, they can encapsulate gas and liquid, thereby being used as drug carriers as well as contrast agents. In addition, ALs can potentially be used to evaluate EPR effects and can be used for molecular delivery of agents under US guidance (6).

In conclusion, the use of ALs and HF-US in combination with the CDSD method has the potential to accurately and noninvasively assess the efficacy of therapies designed to target tumor growth and angiogenesis. In the future, the present method may be used as a new molecular imaging method for assessing angiogenesis, and it can be applied to evaluate antitumor effects by various therapeutic agents.

## Disclosure of Potential Conflicts of Interest

No potential conflicts of interest were disclosed.

## Acknowledgments

The authors thank Yukiko Watanabe and Mizuho Kodama for their technical assistance. CDDP was donated by Nihon Kayaku Co. (Tokyo, Japan).

## Grant Support

T. Kodama received grant-in-aid for scientific research (B) (23300183) and challenging exploratory research (21650124). M. Sakamoto received grant-in-aid for scientific research (B) (21390500) and challenging exploratory research (21659431). S. Mori received grant-in-aid for scientific research (B) (22390378) and challenging exploratory research (22659363) and T. Hayase received support for System Development Program for Advanced Measurement and Analysis (Program-S), JST (6A0901).

The costs of publication of this article were defrayed in part by the payment of page charges. This article must therefore be hereby marked *advertisement* in accordance with 18 U.S.C. Section 1734 solely to indicate this fact.

Received July 19, 2011; revised September 19, 2011; accepted September 20, 2011; published OnlineFirst October 7, 2011.

## References

1. Palmowski M, Huppert J, Hauff P, Reinhardt M, Schreiner K, Socher MA, et al. Vessel fractions in tumor xenografts depicted by flow- or contrast-sensitive three-dimensional high-frequency Doppler ultrasound respond differently to antiangiogenic treatment. Cancer Res 2008;68:7042–9.
2. Sboros V. Response of contrast agents to ultrasound. Adv Drug Deliv Rev 2008;60:1117–36.
3. du Toit LC, Govender T, Pillay V, Choonara YE, Kodama T. Investigating the effect of polymeric approaches on circulation time and physical properties of nanobubbles. Pharm Res 2011;28:494–504.
4. Hitchcock KE, Caudell DN, Sutton JT, Klegerman ME, Vela D, Pyne-Geithman GJ, et al. Ultrasound-enhanced delivery of targeted echogenic liposomes in a novel ex vivo mouse aorta model. J Control Release 2010;144:288–95.
5. Klegerman ME, Wassler M, Huang SL, Zou Y, Kim H, Shelat HS, et al. Liposomal modular complexes for simultaneous targeted delivery of bioactive gases and therapeutics. J Control Release 2010;142:326–31.
6. Kodama T, Aoi A, Watanabe Y, Horie S, Kodama M, Li L, et al. Evaluation of transfection efficiency in skeletal muscle using nano/

Published OnlineFirst October 7, 2011; DOI:10.1158/0008-5472.CAN-11-2389



microbubbles and ultrasound. Ultrasound Med Biol 2010;36: 1196–205.
7. Matsumura Y, Maeda H. A new concept for macromolecular therapeutics in cancer chemotherapy: mechanism of tumoritropic accumulation of proteins and the antitumor agent smancs. Cancer Res 1986;46:6387–92.
8. Suzuki R, Takizawa T, Negishi Y, Hagisawa K, Tanaka K, Sawamura K, et al. Gene delivery by combination of novel liposomal bubbles with perfluoropropane and ultrasound. J Control Release 2007;117:130–6.
9. Funamoto K, Hayase T, Kodama T. Visualization of microcirculation based on brightness variation in contrast-enhanced ultrasound. ASME 2010 Summer Bioengineering Conference; 2010 June 16–19; Naples, Florida; 2010.
10. Kodama T, Tomita N, Horie S, Sax N, Iwasaki H, Suzuki R, et al. Morphological study of acoustic liposomes using transmission electron microscopy. J Electron Microsc (Tokyo) 2010;59:187–96.
11. Aoi A, Watanabe Y, Mori S, Takahashi M, Vassaux G, Kodama T. Herpes simplex virus thymidine kinase-mediated suicide gene therapy using nano/microbubbles and ultrasound. Ultrasound Med Biol 2008;34:425–34.
12. Watanabe Y, Aoi A, Horie S, Tomita N, Mori S, Morikawa H, et al. Low-intensity ultrasound and microbubbles enhance the antitumor effect of cisplatin. Cancer Sci 2008;99:2525–31.
13. Pysz MA, Foygel K, Panje CM, Needles A, Tian L, Willmann JK. Assessment and monitoring tumor vascularity with contrast-enhanced ultrasound maximum intensity persistence imaging. Invest Radiol 2010;46:187–95.
14. U. S. National Institutes of Health. Available from: http://rsbweb.nih.gov/ij/.
15. Stefansson IM, Salvesen HB, Akslen LA. Vascular proliferation is important for clinical progress of endometrial cancer. Cancer Res 2006;66:3303–9.
16. Van der Auwera I, Cao Y, Tille JC, Pepper MS, Jackson DG, Fox SB, et al. First international consensus on the methodology of lymphangiogenesis quantification in solid human tumours. Br J Cancer 2006;95:1611–25.
17. Noguchi Y, Wu J, Duncan R, Strohalm J, Ulbrich K, Akaike T, et al. Early phase tumor accumulation of macromolecules: a great difference in clearance rate between tumor and normal tissues. Jpn J Cancer Res 1998;89:307–14.
18. Dayton PA, Pearson D, Clark J, Simon S, Schumann PA, Zutshi R, et al. Ultrasonic analysis of peptide- and antibody-targeted microbubble contrast agents for molecular imaging of alphavbeta3-expressing cells. Mol Imaging 2004;3:125–34.
19. Lyshchik A, Fleischer AC, Huamani J, Hallahan DE, Brissova M, Gore JC. Molecular imaging of vascular endothelial growth factor receptor 2 expression using targeted contrast-enhanced high-frequency ultrasonography. J Ultrasound Med 2007;26:1575–86.
20. Rayleigh L. The theory of sound. 2nd ed. New York: Dover Publication; 1945.
21. Hoff L, Sontum PC, Hovem JM. Oscillations of polymeric microbubbles: effect of the encapsulating shell. J Acoust Soc Am 2000; 107:2272–80.
22. Medwin H. Counting bubbles acoustically–review. Ultrasonics 1977;15:7–13.
23. Minnaert M. On musical air-bubbles and the sound of running water. Philosophical Magazine 1933;16:235–48.
24. Kelland L. The resurgence of platinum-based cancer chemotherapy. Nat Rev Cancer 2007;7:573–84.
25. Rebillard A, Tekpli X, Meurette O, Sergent O, LeMoigne-Muller G, Vernhet L, et al. Cisplatin-induced apoptosis involves membrane fluidification via inhibition of NHE1 in human colon cancer cells. Cancer Res 2007;67:7865–74.
26. Tan GH, Tian L, Wei YQ, Zhao X, Li J, Wu Y, et al. Combination of low-dose cisplatin and recombinant xenogeneic endoglin as a vaccine induces synergistic antitumor activities. Int J Cancer 2004;112:701–6.
27. Zhong XS, Liu LZ, Skinner HD, Cao Z, Ding M, Jiang BH. Mechanism of vascular endothelial growth factor expression mediated by cisplatin in human ovarian cancer cells. Biochem Biophys Res Commun 2007;358:92–8.
28. Jugold M, Palmowski M, Huppert J, Woenne EC, Mueller MM, Semmler W, et al. Volumetric high-frequency Doppler ultrasound enables the assessment of early antiangiogenic therapy effects on tumor xenografts in nude mice. Eur Radiol 2008;18:753–8.
29. Yancopoulos GD, Davis S, Gale NW, Rudge JS, Wiegand SJ, Holash J. Vascular-specific growth factors and blood vessel formation. Nature 2000;407:242–8.
30. Jain RK. Molecular regulation of vessel maturation. Nat Med 2003;9: 685–93.
31. Xuan JW, Bygrave M, Jiang H, Valiyeva F, Dunmore-Buyze J, Holdsworth DW, et al. Functional neoangiogenesis imaging of genetically engineered mouse prostate cancer using three-dimensional power Doppler ultrasound. Cancer Res 2007;67:2830–9.
32. Iordanescu I, Becker C, Zetter B, Dunning P, Taylor GA. Tumor vascularity: evaluation in a murine model with contrast-enhanced color Doppler US effect of angiogenesis inhibitors. Radiology 2002;222: 460–7.
33. Fleischer AC, Niermann KJ, Donnelly EF, Yankeelov TE, Canniff KM, Hallahan DE, et al. Sonographic depiction of microvessel perfusion: principles and potential. J Ultrasound Med 2004;23:1499–506.
34. Gee MS, Saunders HM, Lee JC, Sanzo JF, Jenkins WT, Evans SM, et al. Doppler ultrasound imaging detects changes in tumor perfusion during antivascular therapy associated with vascular anatomic alterations. Cancer Res 2001;61:2974–82.
35. Lindner JR. Molecular imaging of cardiovascular disease with contrast-enhanced ultrasonography. Nat Rev Cardiol 2009;6:475–81.

Rabieyousefi et al. BMC Immunology 2011, 12:67
http://www.biomedcentral.com/1471-2172/12/67

BMC Immunology

RESEARCH ARTICLE Open Access

# Indispensable roles of OX40L-derived signal and epistatic genetic effect in immune-mediated pathogenesis of spontaneous pulmonary hypertension

Moloud Rabieyousefi[1], Pejman Soroosh[2,7*], Kimio Satoh[3], Fumiko Date[1], Naoto Ishii[2,6], Masahiro Yamashita[1], Masahiko Oka[4], Ivan F McMurtry[4], Hiroaki Shimokawa[3], Masato Nose[5], Kazuo Sugamura[2] and Masao Ono[1,6*]

## Abstract

**Background:** Pulmonary hypertension (PH) refers to a spectrum of diseases with elevated pulmonary artery pressure. Pulmonary arterial hypertension (PAH) is a disease category that clinically presents with severe PH and that is histopathologically characterized by the occlusion of pulmonary arterioles, medial muscular hypertrophy, and/or intimal fibrosis. PAH occurs with a secondary as well as a primary onset. Secondary PAH is known to be complicated with immunological disorders. The aim of the present study is to histopathologically and genetically characterize a new animal model of PAH and clarify the role of OX40 ligand in the pathogenesis of PAH.

**Results:** Spontaneous onset of PAH was stably identified in mice with immune abnormality because of overexpression of the tumor necrosis factor (TNF) family molecule OX40 ligand (OX40L). Histopathological and physical examinations revealed the onset of PAH-like disorders in the C57BL/6 (B6) strain of OX40L transgenic mice (B6.TgL). Comparative analysis performed using different strains of transgenic mice showed that this onset depends on the presence of OX40L in the B6 genetic background. Genetic analyses demonstrated a susceptibility locus of a B6 allele to this onset on chromosome 5. Immunological analyses revealed that the excessive OX40 signals in TgL mice attenuates expansion of regulatory T cells the B6 genetic background, suggesting an impact of the B6 genetic background on the differentiation of regulatory T cells.

**Conclusion:** Present findings suggest a role for the OX40L-derived immune response and epistatic genetic effect in immune-mediated pathogenesis of PAH.

## Background

Pulmonary hypertension (PH) is a severe disease condition that can lead to progressive right ventricular failure and ultimately to death. Pulmonary arterial hypertension (PAH) is a major class of PH defined in the classification of the World Health Organization (WHO). The main histopathological manifestations of PAH are vasoconstriction, endothelial cell proliferation and fibrosis, smooth-muscle cell proliferation, and thrombosis in small pulmonary arteries. These changes result in elevation of pulmonary vascular resistance and, consequently, in pulmonary arterial pressure [1].

PAH occurs as either a primary (idiopathic or familial) or a secondary disease. According to the WHO classification, inflammatory conditions, such as collagen vascular diseases, and viral infections are associated with the occurrence of PAH. Indeed, patients with a subset of idiopathic PAH have some inflammatory disturbances, presented as elevated circulating levels of TNF-α, interleukin (IL)-1, and IL-6 [2]. In the case of severe PAH in humans, infiltration of immune cells, including T cells, B cells, and macrophages, is occasionally observed in pulmonary vascular lesions [3]. Most of the $CD4^+$ and $CD8^+$ T cells infiltrating into the intimal lesions have been

* Correspondence: psoroosh@its.jnj.com; onomasao@med.tohoku.ac.jp
[1]Department of Pathology, Tohoku University Graduate School of Medicine, 2-1 Seiryo, Aoba-ku, Sendai, Miyagi 980-8575 Japan
[2]Department of Immunology, Tohoku University Graduate School of Medicine, 2-1 Seiryo, Aoba-ku, Sendai, Miyagi 980-8575 Japan
Full list of author information is available at the end of the article

shown to express effector memory T-cell markers, indicating the active status of the T cells. In animal models, augmented expression of IL-18 or administration of IL-6 is sufficient to induce mild spontaneous PH [4,5]. In the former case, IL-13 has been shown to critically mediate inflammatory signals in the lung. Recent studies have proposed that naturally arising $CD4^+CD25^+$ regulatory T ($T_{reg}$) cells, or their mediators, may inhibit the development of experimental PH [6]. Furthermore, it has been suggested that the deficiency of $CD4^+$ T cells in humans (e.g., in cases of HIV infection), or the depletion of $CD4^+$ T cells in experimental animal models, is associated with the development of PAH [7]. These observations implicate an immune-mediated mechanism in the development of PAH.

Signals through T-cell costimulatory molecules are critically involved in eliciting optimal T-cell functions [8]. OX40 (TNFRSF4, CD134) is a member of the TNF receptor superfamily that is transiently expressed on activated T cells. The ligand of OX40 (OX40L: TNFSF4, CD134L) is mainly expressed on mature antigen-presenting cells as well as on vascular endothelial cells [9-12]. The OX40-OX40L interaction is required for optimal effector function of T cells [13,14] and generation of memory T cells [15-18]. Recently, growing evidence has unveiled the importance of OX40 signals in the accumulation of effector $CD4^+$ T cells at inflammation sites in mouse models of autoimmune diseases. Moreover, a recent study has demonstrated that constitutive OX40-OX40L interactions in OX40L transgenic mice entail spontaneous development of ulcerative colitis-like disease and an undetermined lung disease, which is accompanied by significant production of an anti-DNA antibody [19]. Interestingly, these pathological manifestations have been observed in mice with the C57BL/6 (B6) genetic background but not in those with the BALB/c (BALB) genetic background. The strain-specific pathological manifestations implicate the presence of a genetic predisposition that modulates OX40L-dependent inflammation in the colon and lungs.

The goal of this study was to characterize the undetermined lung disease presented in an OX40L-transgenic B6 strain (B6.TgL) of mice. In the present study, we proposed a new spontaneous model for PAH. Furthermore, this study provided novel insight into the role of the OX40L-derived signal and the genetic predisposition in the immune-mediated pathogenic mechanism of PAH.

## Methods

### Mice

Mice with OX40L transgene under the expression control of *lck* promoter were generated in a C57BL/6 genetic background as described previously (B6.TgL) [19]. To generate OX40L transgenic mice on BALB/c background (BALB.TgL), B6.TgL backcrossed to BALB/c strains more than 8 times. Age and sex-matched wild-type C57BL/6 and BALB/c were used as controls. For genetic analyses, TgL mice with mixed genetic background were prepared by the mating of BALB × B6.TgL and (BALB × B6) F1 × B6.TgL. All mice were bred and maintained in conventional clean room in the animal department of the Oriental Bio-service, Co. Ltd, Shizuoka, Japan. In all animal experiments in this study, we followed the Tohoku University guidelines for animal experimentation.

### Histopathological examinations

At 20 weeks of age, each mouse was killed under ether anesthesia. The whole lung was immersion fixed in 10% formalin in 0.01 M phosphate buffer (pH 7.2), and embedded in paraffin. Tissue sections were stained with hematoxylin and eosin (H&E) and Masson's trichrome for light-microscopic examination. The disease score of PAH was histopathologically determined. Ten small pulmonary arteries along with terminal bronchioles were individually graded under microscopic examination according to following histopathological criteria: 0, normal; 1, significant, slight thickening of the media; 2, thickening of the media with intimal (endothelial) proliferation and/or fibrosis. A mean grade of all points examined was considered as an individual PAH score. Immunohistochemical analyses were performed using the primary antibodies to human α-smooth muscle actin (αSMA) (DACO, Tokyo, Japan), which has been shown to react mouse αSMA, and mouse CD31 (Santa Cruz Biotechnology, Santa Cruz, CA).

### Right ventricular systolic pressure measurements

B6, BALB, B6.TgL, and BALB.TgL mice were anesthetized by intraperitoneal injection of ketamine hydrochloride (60 mg/kg) and xylazine (8 mg/kg) or, in the second series of measurement using B6, and BALB.TgL mice, pentobarbital sodium (50 mg/kg). Right ventricular systolic pressure (RVSP) was measured in spontaneously breathing mice by direct puncture of the right ventricle with a 25-gauge needle connected to a pressure transducer [20]. In the second series with the pentobarbital anesthetization, it was measured in artificially ventilated mice with median thoracotomy.

### Evaluation of right ventricular hypertrophy

The hearts isolated from B6, BALB, B6.TgL, and BALB.TgL mice were fixed in formalin and dissected into right ventricle (RV), left ventricle (LV), and interventricular septum (IVS). The dissected ventricles were carefully washed in saline to remove blood clots and separately weighted. Right ventricular hypertrophy was evaluated by the weight ratio of RV/(LV+IVS).

### Antibodies and flow cytometric analysis

Anti-CD3-FITC, anti-CD4-allophycocyanin, anti-CD25-allophycocyanin, anti-CD44-phycoerythrin (PE), anti-CD62L-FITC, and anti-IL-17-PE were purchased from BD Biosciences (San Diego, CA). Anti-mouse Foxp3-PE (FJK-16S) was purchased from eBioscience (San Diego, CA). Anti-mouse CD3ε (clone 2C11) used for T cell stimulation and anti-mouse CD16/32 (clone 2.4G2) used for Fc receptor blocking were purified from hybridoma-cultured supernatants in our laboratory. Cells were incubated with antibodies for 30 min at 4°C and then washed to remove unbound antibodies. All the samples were analyzed with a FACSCalibur™ flow cytometer and the CellQuest™ program (BD Biosciences).

### Preparation of lymphocyte culture and cytokine measurements

Single-cell suspensions were prepared from spleen and lungs of an 8 to 10 week-old mouse, in which the lung disease of interest is not developed. Lymphocytes in the lung were obtained by digesting minced lung tissues with 150 U/ml collagenase (Maeda Co. Ltd., Tokyo, Japan) as described previously [21]. The number of effector/memory and regulatory T cells were calculated based on the percentage of each subpopulation that was $CD44^{high}CD62L^{low}$ and $CD4^{+}Foxp3^{+}$, respectively, and the total cell number in each organ. Total lymphocytes isolated from lung tissues that contained equal number of effector/memory $CD4^{+}$T cells (normalized based on absolute number of effector/memory CD4 T cells) were stimulated with soluble anti-CD3ε (10 μg/ml) at 37°C for the indicated time. IL-13 levels were assayed in cultured supernatants using ELISA kit for IL-13 (R&D Systems, Minneapolis, MN), according to the manufacturer's recommendations. The production of IL-17 in lymphocytes was detected by intracellular staining with anti-IL-17-PE following incubation of lymphocytes for 4 h with 50 ng/ml PMA, 500 ng/ml Ionomycin (Sigma-Aldrich, St. Louis, MO) in the presence of 10 μg/ml brefeldin A (Invitrogen, Carlsbad, CA).

### Genetic mapping

Genotypes of BCN2.TgL mice were determined by polymerase chain reaction (PCR) using genomic DNA prepared from the tail tip. The genotyping PCR was performed using standard reagent and the following conditions: 94°C for 5 min, 35 cycle of 94°C for 30 sec, 58°C for 30 sec, 72°C for 30 sec, and final extension 72°C for 5 min with the 98 microsatellite markers (additional file 1), which represent amplified fragment-length polymorphism between BALB and B6 strains. This genotyping provided full coverage of the mouse autosomes with the marker spaced an average of 12.5 cM apart and a maximum distance of 35 cM between any two markers. PCR products were visualized with electrophoresis on 2-4% agarose gels containing 0.01% ethidium bromide.

In a genome-wide scan, we determined genotypes of the 48 BCN2.TgL mice, which were selected as the top (severest) 24 and the bottom 24 on the list of PAH score, at all the 98 microsatellite positions (additional file 1) . The association at each microsatellite position was evaluated with chi-square test for independence between the genotypes and the two groups that were positive and negative for the incidence of PAH, using standard 2 × 2 contingency matrices. A $p$ value less than 0.05 was regarded as suggestive association. The suggestive association was confirmed by the two-tail $t$-test for the difference of means between the two genotype groups of a total of 341 BCN2.TgL mice. In this test a $P$ value less than 0.0034 was regarded as suggestive association. This P threshold was referred to the previous recommendation [22].

In a linkage mapping, a linkage position was determined with the quantitative trait locus (QTL) program. The logarithm of odd (LOD) was determined with the interval mapping program in the Windows QTL Cartographer (V2.5) software. The PAH scores of all BCN2.TgL mice were used as an indicator of phenotype. A suggestively significant level ($\alpha$ = 0.05) of LOD was determined by the permutation test installed in this software (1000 permutations). Map positions (cM) of the microsatellite makers were based on the information of the Mouse Genome Database of The Jackson Laboratory (http://www.informatics.jax.org).

### Statistics

A 95% confidence interval shown in Table 1 was calculated using the method described previously [23]. The two-tailed $t$-test was used to evaluate a difference of

**Table 1 Summary of PAH scores of B6, BALB, and transgenic strains of mice**

| Mice* | | n† | Median of score | 95% CI‡ | Statistics§ |
|---|---|---|---|---|---|
| B6 | | 9 | 0 | 0 - 0.1 | |
| BALB | | 2 | 0 | n.d. | |
| B6. TgL | | 15 | 0.7 | 0.35 - 1.05 | ¶ |
| BALB. TgL | | 8 | 0 | 0 - 0.1 | |
| BCF1. TgL | | 30 | 0.05 | 0 - 0.1 | |
| BCN2. TgL | female | 174 | 0.25 | 0.2 - 0.4 | ¶ |
| BCN2. TgL | male | 167 | 0.25 | 0.2 - 0.4 | ¶ |

* All mice were killed at 20 week-old for this examination. BCF1, BALB × B6; BCN2, BCF1 × B6.TgL.

† Number of mice tested.

‡ CI, confidential interval. The CI was not determined (n.d.) for BALB/c (BALB).

§ The significance of this study was evaluated by Mann-Whitney U-test for the all strains.

¶, P < 0.01 (v.s. B6).

means between two groups. A $P$ value less than 0.05 considered as significant.

## Results

### Histopathological characterization of the lung phenotype

Microscopic examination revealed diffuse pathological changes in the small- to medium-sized pulmonary arteries in B6.TgL (Figure 1A, E), but not in B6 (Figure 1B), BALB strain of OX40L transgenic mice (BALB.TgL) (Figure 1C), or BALB (Figure 1D). This vascular lesion was found to be readily accompanied with perivascular infiltration of lymphocytes and, to a lesser extent, neutrophils (Figure 1F). These changes were mainly observed in arteries contained in bronchovascular bundles (respiratory arteries) and were typically characterized by fibrocellular endothelial proliferation of the intimal layer and, to a lesser extent, medial muscular hypertrophy (Figure 1G and 1H). Neither muscularization of distal pulmonary arterioles, which is a common pathological change in a hypoxic PAH model, nor plexiform lesions, found in human PAH, were identified. The cells in the intimal lesion were characterized as positive for a myofibroblast marker, smooth muscle-specific actin (αSMA) (Figure 1I), and an endothelial cell marker, CD31 (Figure 1J). When no treatment was administered to avoid vasospasm before the histopathological preparation, vasoconstriction was frequently observed in pulmonary arteries of B6.TgL but not in wild-type B6, BALB, and BALB.TgL mice, irrespective of the presence of the overt pathological changes mentioned above (data not shown). Perivascular lymphocytic infiltration was also observed around pulmonary veins; however, there was no pathologic remodeling in those veins as observed in the

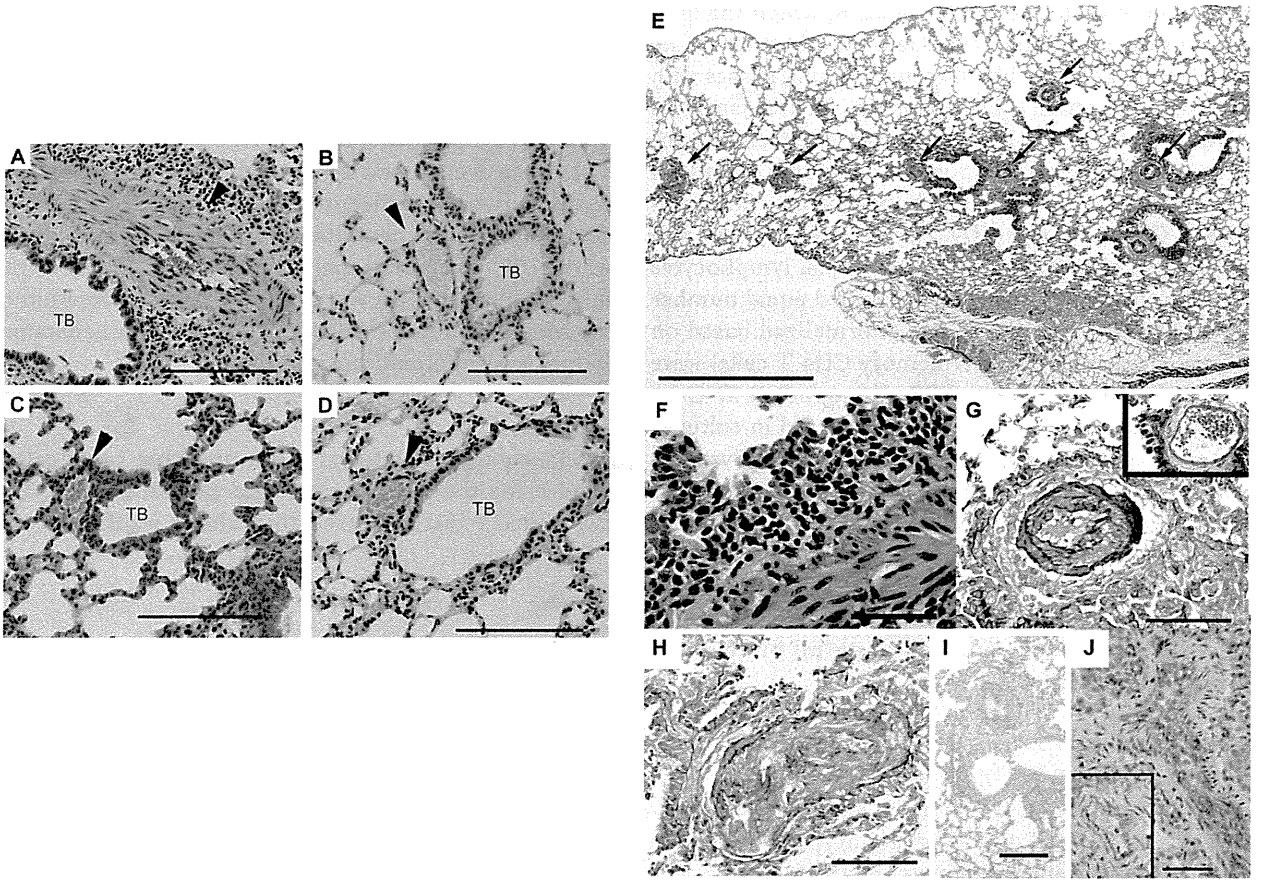


**Figure 1 Histopathological features of the lung disease in B6**.TgL mice. (A-D) Histopathological manifestation typically present in B6.TgL (A). No pathological manifestation observed in B6 (B), BALB.TgL (C), and BALB (D). The photograms indicated were taken from over 20-week aged male mouse. Arrow heads indicate pulmonary arteries. *TB*, terminal bronchiole. H&E staining. Scale bar = 100 μm. (E) Diffuse pathology present in B6.TgL. Masson's trichrome staining. Scale bar = 1 mm. (F) Perivascular lymphocytic infiltration in the affected lung. H&E staining. Scale bar = 50 μm. (G, H) Representative microscopic appearance in the affected arteries in the B6.TgL lung. An inset photogram in *G* represents the appearance of a normal pulmonary artery. Thickening of the intimal and, to a lesser extent, medial layers with marked intimal fibrosis is characteristic of the affected arteries. Masson's trichrome staining. Scale bar = 100 μm. *I* and *J*, expression of αSMA and CD31 (PECAM), respectively in the thickened arterial wall. The photogram in the inset of *J* represents a normal manifestation of unaffected artery. Immunohistochemical staining with hematoxylin counter-staining. Scale bar: in *I*, 200 μm; in *J*, 100 μm.

arteries (data not shown). Degenerative or granulomatous vascular lesions were not observed in conjunction with the perivascular infiltration, indicating that the vascular lesion of interest is not related to any type of vasculitis syndrome. We found no vascular lesions in the kidney or the colon of B6.TgL mice. Thus, the spontaneous lung disease in B6.TgL mice was characterized by lung-specific, pulmonary artery-restricted intimal thickening with lymphocytic (chronic) inflammation. These histopathological characteristics are similar yet distinct in a few points from those of human PAH.

### Strain-restricted onset of the lung disease

The PAH-like disease, as defined in the B6.TgL mice, was quantified with a PAH score in other strains of mice, including B6, BALB, BALB.TgL, BALB × B6.TgL (BCF1.TgL), and (BALB × B6) F1 × B6.TgL (BCN2.TgL). It was observed that wild-type and different TgL strains, such as BALB.TgL and BCF1.TgL, barely developed the PAH-like disease (Table 1). On the other hand, BCN2.TgL developed a PAH-like disease with a broader distribution of the PAH score than B6.TgL. There were no sex-related differences in the PAH scores (Table 1). These findings indicate that development of the PAH-like disease depends on both the effects of TgL and on an undefined B6-specific genetic background.

### Elevation of RV systolic pressure and RV hypertrophy in B6.TgL

The PAH-like arteriopathy in B6.TgL mice indicated the onset of clinical PH. We therefore measured right ventricular (RV) systolic pressure (RVSP) in aged B6.TgL, BALB.TgL, and their wild-type strains. RVSP was significantly increased in the B6.TgL mice, as compared to B6 (Figure 2A). Importantly, the RVSP values were significantly correlated with the PAH scores (Figure 2B). Furthermore, significant RV hypertrophy was demonstrated for B6.TgL, as compared to B6 mice (Figure 2C). Increases in RVSP and RV hypertrophy were not observed in the BALB.TgL mice, as compared to B6 mice (additional file 2). In other experiments performed using wild-type BALB mice (30 w), there has been no evidence for RV hypertension or RV hypertrophy in BALB strain: RVSP = 21.3 ±2.72 mmHg, RV/(LV + IVS) = 0.25 ±0.026.

### Accumulation of effector/memory $CD4^+$ T cells in OX40L-Tg mice

Previous studies performed with B6.TgL mice have demonstrated a selective increase in the number of $CD44^{high}CD62L^{low}$ effector/memory $CD4^+$ T cells in lymphoid and nonlymphoid tissues [17,19]. We examined whether the tissue distribution of effector/memory $CD4^+$ T cells was altered by the genetic background before the disease onset. Flow cytometric analyses revealed a significant increase in the number of effector/memory $CD4^+$ T cells in both the spleen (Figure 3A and 3B) and lungs (Figure 3C and 3D) in every TgL mouse examined. Importantly, this increase was not observed in a strain-specific manner, indicating that the development of PAH is not simply explained by the increase of effector/memory $CD4^+$ T cells.

### Strain-specific profile of cytokine production by the lung $CD4^+$ T cells

The functionality of resident $CD4^+$ T cells in the lungs of TgL mice was determined by testing their ability to produce cytokines in response to anti-CD3 or PMA/ionomycin stimulation, respectively. Augmented IL-13 production was observed in the TgL-derived T cells and interestingly, this augmentation was greater in B6.TgL than in BALB.TgL (Figure 4A). Furthermore, a larger number of IL-17-producing $CD4^+$ T cells were observed in B6.TgL mice than in BALB.TgL (Figure 4B). IL-4 and IL-5 were not detected in stimulated lung cells by any strains (data not shown). These results indicate that the function of tissue resident CD4 T cells can be modulated by the excessive OX40 signals on B6 genetic background before disease onset.

### Over-expression of OX40L in B6 background alters the balance between lung resident effector/memory T cells and regulatory T cells

$CD4^+CD25^+Foxp3^+$ T cells, usually denoted as $T_{reg}$ cells, are known to control inflammatory responses by suppressing the activities of $Foxp3^-$ effector T cells [24]. Several independent studies have demonstrated that lung resident $T_{reg}$ cells suppress type 2 immune responses and, consequently, reduce pulmonary inflammation [25-27]. We analyzed the population size of $T_{reg}$ cells, defined as $CD4^+Foxp3^+$, in the lung of non-transgenic and TgL strains. Flow cytometric analyses revealed that the frequency and absolute number of $T_{reg}$ cells increased in TgL strains in advance of the disease onset as compared with those in nontransgenic strains (Figure 5A and 5B). It was particularly noted that the increase of $T_{reg}$ was less in B6.TgL than in BALB.TgL, suggesting that B6-specific genetic factors counteract development of $T_{reg}$ cells in TgL mice. We also examined the ratio of Foxp3- effector/memory CD4 T cells (additional file 3) to Foxp3+ $T_{reg}$ before disease onset. The data shows an increased ratio of effector/memory T cells to $T_{reg}$ cells in the B6.TgL lung compared to the BALB.TgL lung (Figure 5C). These findings also suggest an important role of $T_{reg}$ in regulating inflammation associated with the pathogenesis of PAH-like disease in B6.TgL mice.

### Identification of a susceptibility locus for PAH

TgL-dependent PH developed in a strain-specific manner, suggesting that the genetic background had an effect

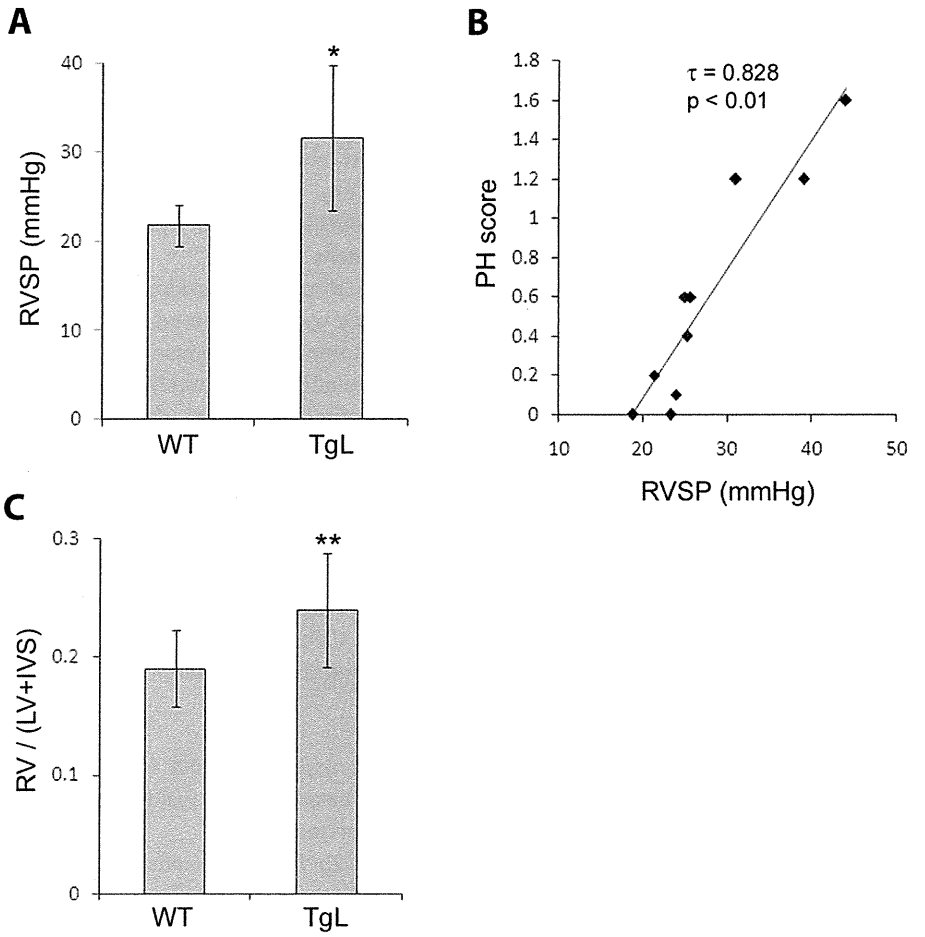


**Figure 2 Clinicopathological phenotypes associated with PH.** (A) Significant elevation of RVSP (mmHg) in B6.TgL. The result represents a mean ± standard deviation (SD) of 4 B6 or 6 B6.TgL mice (20 to 24 weeks old) for each group. (B) Correlation between RVSP values and PAH scores obtained from the 10 mice examined in *A*. The significance of this correlation was confirmed with the Kendall tau ($\tau$) rank correlation coefficient ($\tau$ = 0.828). (C) RV hypertrophy manifested in B6.TgL. RV hypertrophy was evaluated with the index provided by the formula, RV/(LV+IVS). The result represents a mean ± SD of 12 B6 or 8 B6.TgL mice for each group. The significant difference between the two groups was evaluated by two-tailed *t*-test. *, $p < 0.05$; **, $p < 0.01$.

on the disease phenotypes. To identify a susceptibility locus for a PAH-like disease in B6.TgL, a genetic approach was employed using BCN2.TgL mice, which are descended from the B6.TgL and non-disease-prone BALB.TgL strains of mice. A genome-wide scan performed using selected 48 BCN2.TgL mice identified 4 candidate loci on chromosomes 5, 9, 13, and 17, which were possibly associated with the incidence of a PAH-like disease (additional file 1). The association study with 341 BCN2.TgL mice confirmed the suggestive association at *D5Mit346* (1 cM) and *D5Mit381* (8 cM) on chromosome 5 (Table 2). The other candidate loci preliminarily defined on chromosomes 9, 13, and 17 were not confirmed by this study. A QTL analysis consistently demonstrated a suggestive linkage between the level of PAH score and the chromosomal region between *D5Mit346* and *D5Mit381*. This linkage was observed in a single LOD peak of 2.4 at 7 cM on chromosome 5 (Figure 6).

## Discussion

Previous studies have shown that B6.TgL mice display abnormal T-cell differentiation and functions, and spontaneous inflammation in the colon and lung. The colonic phenotype in B6.TgL mice was histopathologically defined as an inflammatory bowel disease resembling ulcerative colitis in humans. In the present study, the undetermined lung disease in B6.TgL mice was characterized as a PAH-like disease. PAH is a clinical category of PH that comprises many different disease entities. Pathological manifestations of the PAH-like disease in B6.TgL mice are not completely parallel to those of idiopathic PAH. The differences between idiopathic PAH

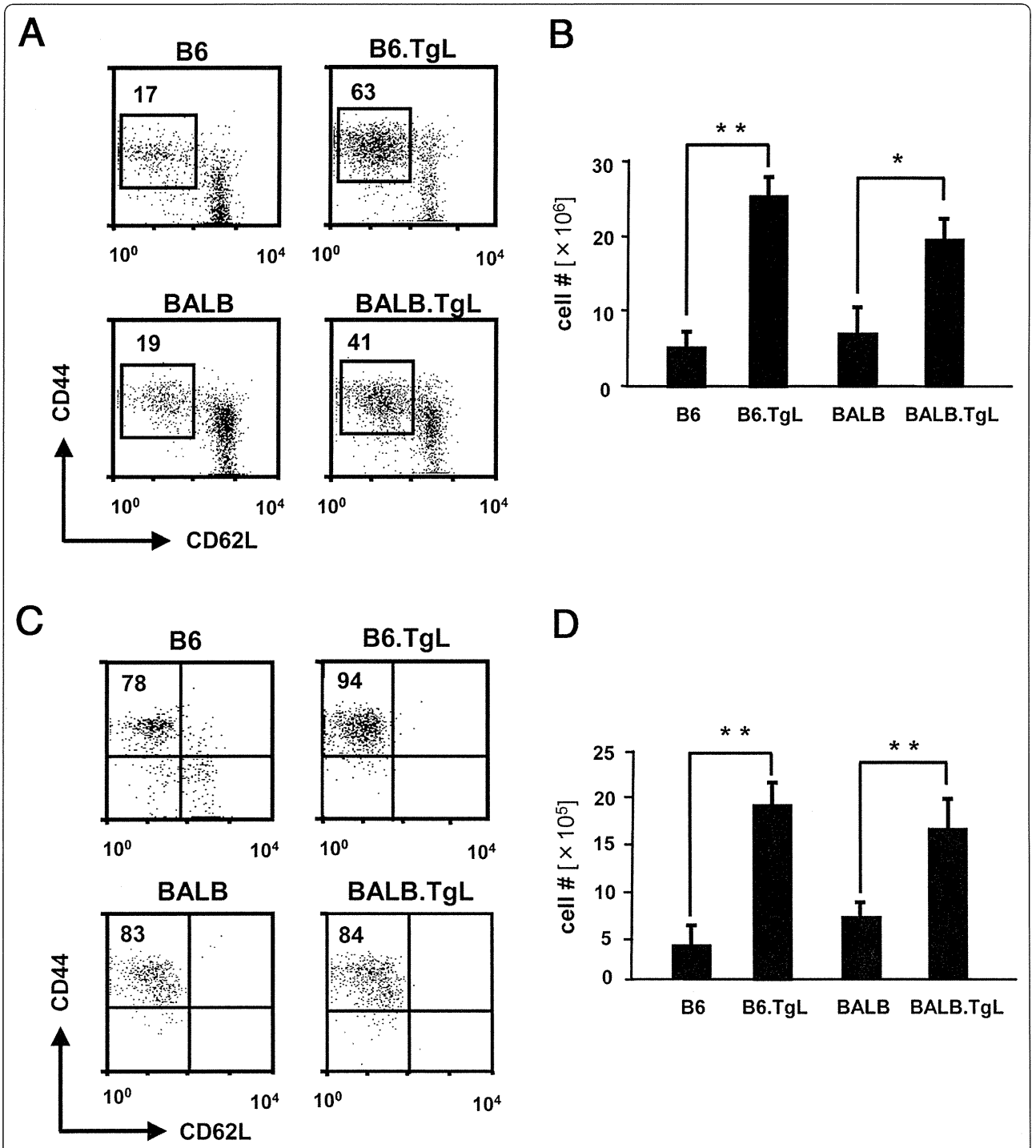


**Figure 3 Accumulation of effector/memory CD4$^+$ cells in transgenic (TgL) strains of mice**. The percentages of CD44$^{high}$CD62L$^{low}$CD25$^-$CD4$^+$ T cells (effector/memory CD4$^+$T cells) in a total of CD4$^+$T cells are shown in the dot grams; (A) spleen, (C) lung. The absolute numbers of effector/memory CD4$^+$ T cells are shown in the bar grams; (B) spleen, (D) lung. The absolute number was calculated from the percentage of this subset and the total cell number in each organ. The results represent a mean ± SD of 6-8 mice per each group. The results of flow cytometry (A and C) are representative of three independent experiments performed using 8 to 10 week-old mice. The significant difference between the two groups was evaluated by two tailed *t*-test. *, $p < 0.01$; **, $p < 0.001$.

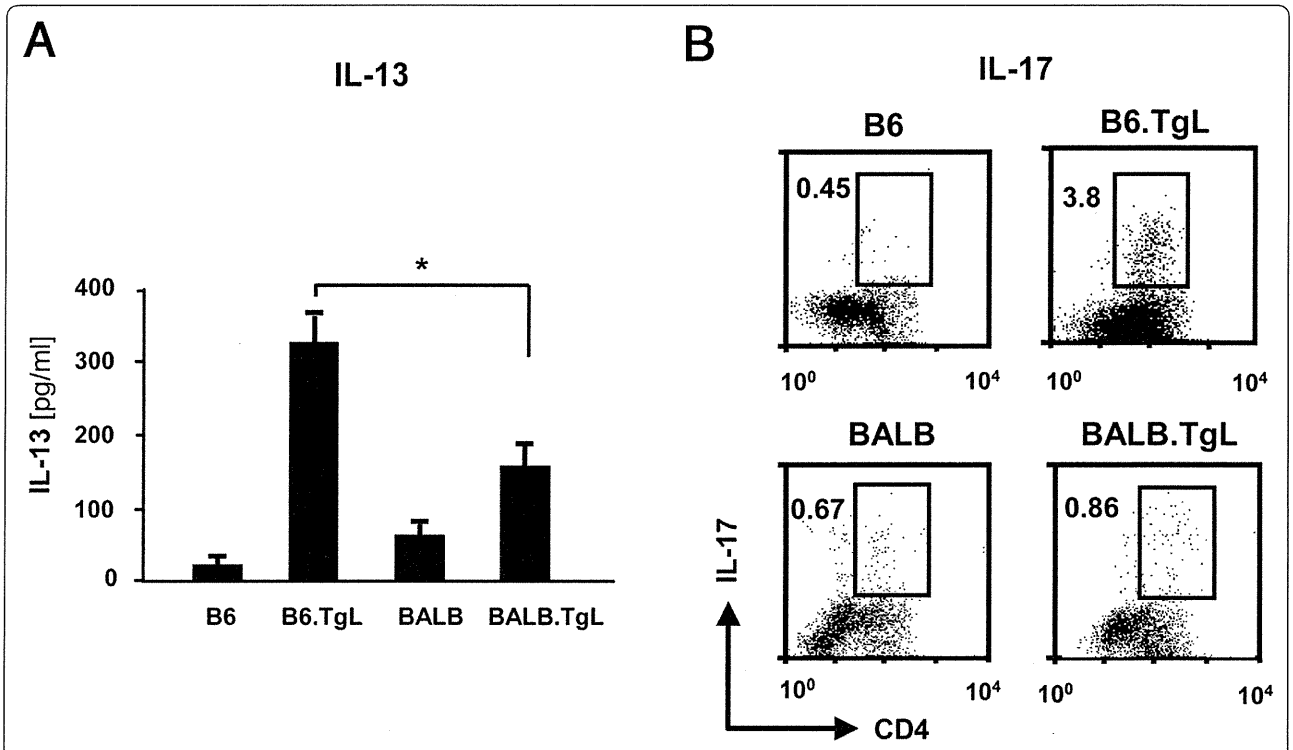


**Figure 4 Strain-specific cytokine profile in lung CD4$^+$T cells.** (A) IL-13 production from a total of lymphocytes isolated from the lung of non-transgenic and transgenic (TgL) strains of mice at 8 to 10 week-old. Lymphocytes containing equal number of CD44$^{high}$CD62L$^{low}$CD4$^+$T cells for each group (n = 4) of strain were stimulated with soluble anti-CD3 for 48 h and IL-13 in the cultured supernatant was quantified by ELISA. The significant difference between B6.TgL and BALB.TgL was evaluated by two-tailed *t*-test. *, $p < 0.05$. (B) IL-17 production in the lung CD4$^+$T cells. Lymphocytes isolated as above were incubated with PMA/Ionomycin in the presence of brefeldin A for 4 h and intracellular IL-17 production was analyzed in CD4 T cells. Representative data from two independent experiments were shown.

and the present animal model include the caliber of the affected arteries, the primarily affected layer of vascular wall, and the participation of massive lymphocytic perivascular infiltration. Further investigations are needed to define the present lung pathology as any type of PAH. An increasing body of evidence implicates the role of immune-mediated mechanisms in the pathogenesis of PAH. A type of PAH occurs secondarily to collagen vascular disorders, such as systemic sclerosis and mixed connective tissue disease (MCTD). Interestingly, PAH with MCTD presents with a prominent characteristic of endothelial degeneration and proliferation, probably due to the pathogenic contribution of autoantibodies to endothelial cells [28,29]. This characteristic may be a pathological consequence of immune-mediated mechanisms shared with the present model. The findings in the B6.TgL mice provide a possible insight into an implication of an OX40L-derived signal in the immune-mediated mechanism of endothelial pathology in PAH.

PAH is associated with endothelial cell dysfunction and vasoconstriction. There is no direct evidence for a link between these pulmonary vascular manifestations and abnormality *in situ* of OX40L-derived signal. However, it has been shown that OX40L-derived signals have a pathologic impact on the endothelial cell functions of systemic arteries. Recent studies have demonstrated an association of OX40L gene polymorphism with the susceptibility to atherosclerosis in humans [30], and the critical contribution of OX40-OX40L interactions to atherogenesis in low-density lipoprotein receptor-deficient mice [31]. The endothelial cells of the systemic arteries and those of the pulmonary arteries are exposed to different conditions, i.e., blood pressure and oxygen tension. It is interesting to know whether the OX40-OX40L interactions yield a different response on pulmonary endothelial cells than on systemic endothelial cells, and whether the OX40L gene polymorphism is associated with any type of PAH in humans.

Our present immunological studies performed using TgL and non-TgL strains of mice with different genetic backgrounds–B6 and BALB–revealed the respective effects of TgL and strain-dependent genetic background on immune phenotypes in the lung. Previous studies have demonstrated that OX40L-derived signals promote the expansion of effector/memory CD4$^+$ T cells [17,19]

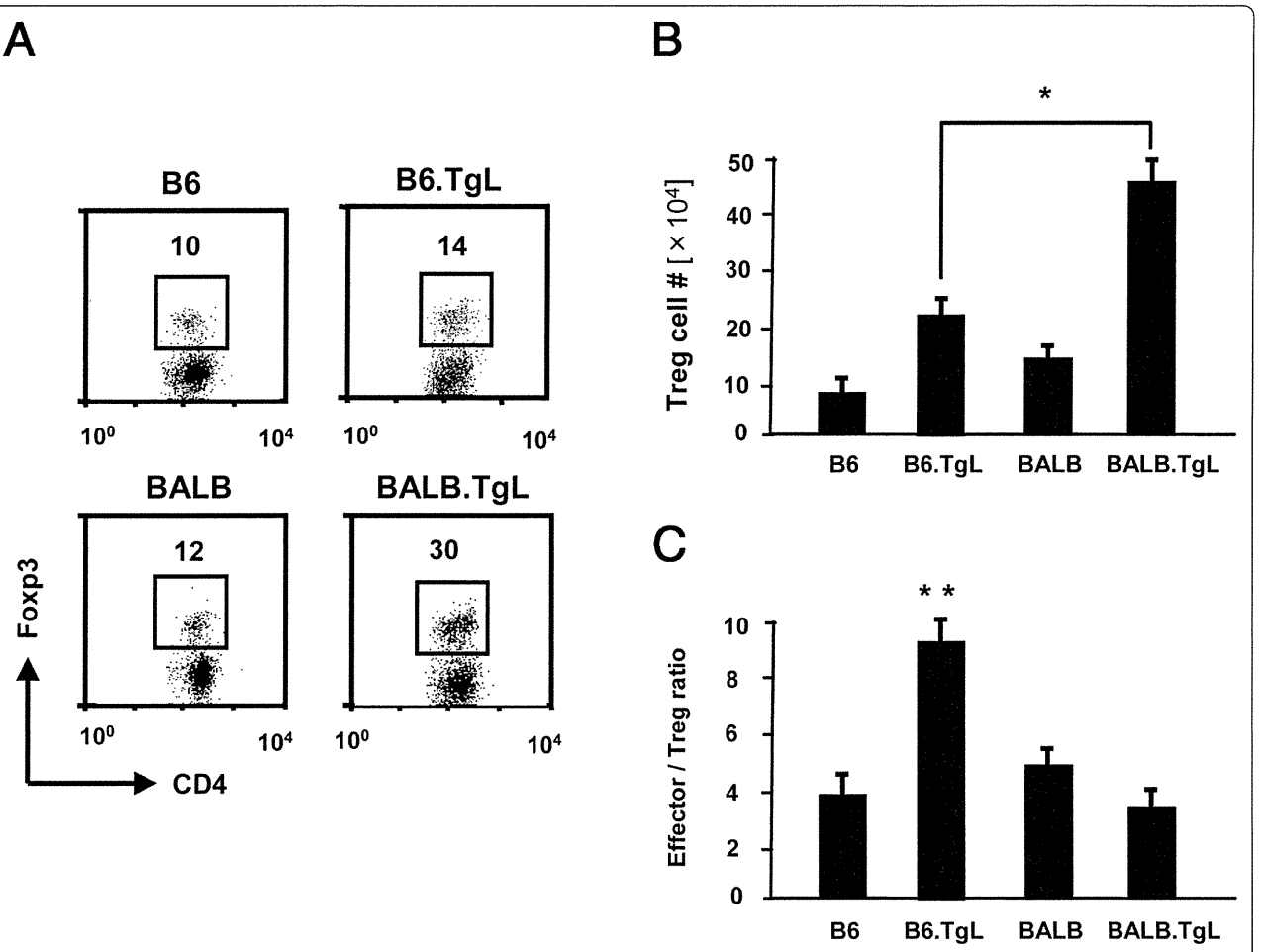


**Figure 5 Accumulation of $T_{reg}$ cells in non-transgenic and transgenic (TgL) strains of mice at 8 to 10 week-old**. The percentage (A) and absolute numbers (B) of $CD4^+$ $Foxp3^+T_{reg}$ cells in the lung are shown. The absolute lymphocytic number was calculated from the percentage of $T_{reg}$ and the total cell number. (C) The ratio of effector/memory T cells (CD4+ CD25- CD44 $^{high}$ CD62L $^{low}$) to Fopx3+ $T_{reg}$ cells in the lung. A significant increase in this ratio is shown in B6.TgL strain of mice. The result represents a mean ± SD from 4 mice per each group. The results of flow cytometry (A) are representative of two independent experiments. The significant difference between the two groups was evaluated by two tailed *t*-test. *, $p < 0.01$; **, $p < 0.001$.

and naturally arising $T_{reg}$ cells [32], and enhance the production of IL-13 and IL-17 by $CD4^+$ T cells [33-35]. To examine which TgL-dependent immune aberrations are correlated with the onset of the PAH-like disease, we examined TgL-dependent immune phenotypes in the lungs of 2 different strains at a pre-disease stage. The findings indicate that B6-specific genetic factors influence the expansion of effector/memory $CD4^+$ T cells and $T_{reg}$ cells in advance of the onset of lung disease. A possible role of $T_{reg}$ cells has been documented in the

**Table 2 Genetic association of PAH score in BCN2**

| Marker | Position (CM) | Mean of grade† BB | Mean of grade BC | P value‡ |
|---|---|---|---|---|
| D5Mit346 | 1 | 0.51 ± 0.61 (172) | 0.32 ± 0.46 (169) | 0.0018 § |
| D5Mit381 | 8 | 0.51 ± 0.59 (178) | 0.32 ± 0.46 (163) | 0.0012 § |
| D5Mit197 | 36 | 0.46 ± 0.56 (192) | 0.36 ± 0.52 (149) | 0.0844 |
| D5Mit338 | 59 | 0.45 ± 0.55 (191) | 0.37 ± 0.53 (150) | 0.1476 |
| D5Mit213 | 70 | 0.41 ± 0.52 (192) | 0.42 ± 0.58 (149) | 0.9149 |
| D5Mit409 | 83 | 0.42 ± 0.55 (165) | 0.41 ± 0.54 (178) | 0.766 |

* Values indicate mean ± SD and the values in parenthesis denote the number of mice.

† BB = B6 homozygote; BC = B6/BALB heterozygote

‡ The two-tail t-test. §, suggestive linkage [22].

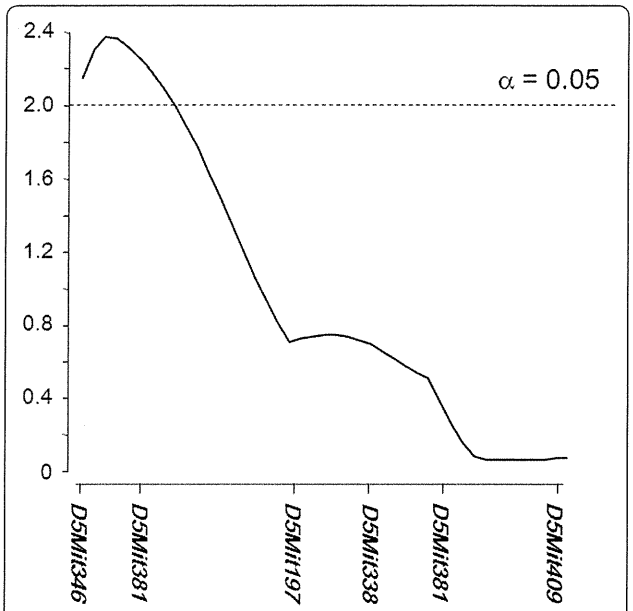


**Figure 6 LOD plots of the QTL analysis for PAH scores on chromosome 5.** The significant threshold level ($\alpha = 0.05$) is shown by a score of 2 with a dashed line. The LOD peak (2.4) is located at 7 cM. The Y-axis denotes the level of the LOD score, and the X-axis denotes the genetic position defined by the microsatellite markers indicated: *D5Mit346* (1 cM), *D5Mit381* (8 cM), *D5Mit197* (36 cM), *D5Mit338* (59 cM), *D5Mit213* (70 cM), and *D5Mit409* (83 cM). The results were obtained using the interval mapping program of the MapMarker/QTL software.

development of PAH in humans [6]. Furthermore, it is clearly shown that B6-specific genetic factors increase the number of IL-17-producing $CD4^+$ T cells as well as secretion of IL-13 and IFNγ (data not shown) by lung tissue resident $CD4^+$ T cells. IL-17 producing CD4 T cells, namely Th17 cells are well known that participates in the pathogenesis of various organ-specific autoimmune diseases, such as inflammatory bowel disease and rheumatoid arthritis [36,37]. Although the role of Th17 cells in PAH in humans has not been determined, our present findings suggest that they indeed play a role in PAH. IL-13 serves as an important mediator in pulmonary inflammation [5,38,39], suggesting a causal contribution of IL-13 to the pathogenesis of the present model. The presence of immunological findings provides an insight into PAH-prone immune condition in the lung: the increase of proinflammatory effectors, IL-13 and Th17, and the decrease of an anti-inflammatory effector, $T_{reg}$.

The present genome-wide genetic approach demonstrated a new susceptibility locus controlling the onset of a PAH-like disease in our model. Previous genetic studies performed on familial PAH have shown mutations in 2 genes responsible for susceptibility to PAH: bone morphogenetic protein receptor 2 gene (*BMPR2*) [40] and activin-like kinase type-1 gene (*ALK-1*) [41]. Our identified locus includes neither of these genes, nor, to the best of our knowledge, any gene involved in their signal transduction pathways. However, *Nos3* and *Hgf* genes were particularly noted within this locus. Nitric oxide (NO) is known as a potent endothelial cell-derived vasodilator and an inhibitor of smooth muscle proliferation. Endothelial NO production largely depends on NOS3/eNOS (encoded by *Nos3*). NOS3-deficient mice showed reduced pulmonary vascular proliferation and remodeling to chronic hypoxia [42,43]. Several studies have reported the preventive role of NO in the development of PH in mice and humans. The polymorphism of human *Nos3* gene is associated with high-altitude pulmonary edema and PH in patients with chronic obstructive pulmonary disease [44]. On the other hand, *Hgf*, which encodes hepatocyte growth factor (HGF), suppresses vascular medial hyperplasia and matrix accumulation in advanced PH in rats [45]. These findings have underscored the role of NOS3/eNOS or HGF as a pathogenic modifier in the present PH model.

A T-cell subset, type II helper T cell (Th2), plays an important role in the pathogenesis of PAH in mice [39]. In this regard, it is noteworthy that the 2 loci (the transgene locus and the susceptibility locus) have a strong impact on Th1/Th2 balance. The OX40 signal promotes a Th2-prone condition in mice [34]. On the other hand, NO and HGF serve as inducible factors for type I helper T cells (Th1) [46,47]. Therefore, in the TgL strains of mice, the 2 loci are mutually counterbalanced, and the net Th1/Th2 proportion depends mainly on the polymorphic effect of the susceptibility locus. In a B6 genetic background, an effect of the susceptibility locus may suppress Th1 responses and maximize Th2 augmentation in the lung conferred by the OX40L transgene, resulting in the B6-specific onset of PH.

## Conclusion

The present study reported a novel transgenic mouse model for PH. This model differs from previous PH models, which include a hypoxia-induced model, a drug-induced model, and a genetic model (i.e., endothelin B receptor-deficient) [48], in etiology, histopathology, and spontaneity of PH. Considering the physiological functions of OX40L, it is likely that the development of PH in the present model depends on Th2-mediated mechanisms. The present model may provide a new experimental opportunity for investigating immune-mediated mechanisms underlying PAH and the development of immune-targeted therapy for PAH.

## Additional material

**Additional file 1: Summary of genome wide scan.** Genotypes of BCN2.TgL mice were determined by polymerase chain reaction (PCR) using genomic DNA for 98 microsatellite positions.

**Additional file 2: Pathological phenotypes in the lung of BALB.TgL mice**. (A) RVSP (mmHg) in BALB.TgL (35 w, male, n = 4) and wild-type B6 (28 w, male, n = 4). The difference in the average values between the two strains is not statistically significant (p = 0.37, two tailed t test). These RVSP values tended to be lower than those in our previous measurement shown in Figure 2A. This change is probably due to the difference in the experimental conditions. (B) Evaluation of RV hypertrophy in BALB.TgL (35 w, male, n = 5) and wild-type B6 (28 w, male, n = 5). RV hypertrophy was evaluated with the index of RV/(LV +IVS). The difference between the two strains is not statistically significant (p = 0.76, two-tailed t-test).

**Additional file 3: Foxp3 expression on total CD4 versus CD25 negative effector CD4 T cells**. Total CD4 and CD4+CD62L$^{low}$CD25 negative cells from the lung tissue were stained for intracellular Foxp3.

### List of Abbreviations

αSMA: Alpha smooth muscle actin; B6.TgL: OX40L transgenic on C75BL/6 strain; BALB. TgL: OX40L transgenic on BALB/c strain; H & E: Hematoxylin and Eosin; HGF: Hepatocyte growth factor; IVS: Intraventricular Septum; LOD: Logarithm of odd; LV: Left ventricular; MCTD: Mixed connective tissue disease; NO: Nitric oxide; OX40L: OX40 ligand; PH: Pulmonary hypertension; PAH: Pulmonary arterial hypertension; PMA: phorbol 12-myristate 13-acetate; QTL: quantitative trait locus; RV: Right ventricle; RVSP: Right ventricular systolic pressure; Th: T helper cells; T reg: regulatory T cell; TNFSF: Tumor necrosis super-family

### Acknowledgements

We would like to thank Drs. Mingcai Zhang, Hiroshi Furukawa, Hiroyuki Kumagai, Shigeki Shibahara, Yasushi Hoshikawa, and Masahisa Kyogoku for providing helpful, critical comments, Mr. Shin-ichi Tanaka and Miss Naomi Yamaki for technical help in the RVSP measurement, and Mrs. Emi Yura for secretarial help. This work was supported by grants: No.19390108 & No.19659096, Grants-in-Aid for Scientific Research from the Ministry of Education, Science, Sports, and Culture of Japan. CREST, JST.

### Author details

[1]Department of Pathology, Tohoku University Graduate School of Medicine, 2-1 Seiryo, Aoba-ku, Sendai, Miyagi 980-8575 Japan. [2]Department of Immunology, Tohoku University Graduate School of Medicine, 2-1 Seiryo, Aoba-ku, Sendai, Miyagi 980-8575 Japan. [3]Department of Cardiovascular Medicine, Tohoku University Graduate School of Medicine, 2-1 Seiryo, Aoba-ku, Sendai, Miyagi 980-8575 Japan. [4]Department of Pharmacology and Medicine and Center for Lung Biology, University of South Alabama, College of Medicine, 307 University Blvd N Mobile, AL 36688-0002 USA. [5]Department of Pathology, Ehime University Graduate School of Medicine, Shitsukawa, Toon, Ehime 791-0295 Japan. [6]Japan Science and Technology Agency, CREST, Tokyo, Japan. [7]Johnson & Johnson Pharmaceutical Research & Development, L.L.C., 3210 Merryfield Row, San Diego, California 92121, USA.

### Authors' contributions

MR and MO (Ono) conceived the project and contributed to all the aspect of this research. MN contributed to the genetic findings. MY, MO (Oka), and IFM contributed to histopathological findings. PS, NI, and KS (Sugamura) contributed to immunological findings. KS (Satoh) and HS contributed to physical findings such as blood pressure measurements. All authors read and approved the final manuscript.

### Competing interests

The authors declare that they have no competing interests.

Received: 16 June 2011 Accepted: 15 December 2011
Published: 15 December 2011

### References

1. Veeraraghavan S, Koss MN, Sharma OP: **Pulmonary veno-occlusive disease.** *Curr Opin Pulm Med* 1999, **5(5)**:310-313.
2. Dorfmuller P, Perros F, Balabanian K, Humbert M: **Inflammation in pulmonary arterial hypertension.** *Eur Respir J* 2003, **22(2)**:358-363.
3. Humbert M, Morrell NW, Archer SL, Stenmark KR, MacLean MR, Lang IM, Christman BW, Weir EK, Eickelberg O, Voelkel NF, *et al*: **Cellular and molecular pathobiology of pulmonary arterial hypertension.** *J Am Coll Cardiol* 2004, **43(12 Suppl S)**:13S-24S.
4. Golembeski SM, West J, Tada Y, Fagan KA: **Interleukin-6 causes mild pulmonary hypertension and augments hypoxia-induced pulmonary hypertension in mice.** *Chest* 2005, **128(6 Suppl)**:572S-573S.
5. Hoshino T, Kato S, Oka N, Imaoka H, Kinoshita T, Takei S, Kitasato Y, Kawayama T, Imaizumi T, Yamada K, *et al*: **Pulmonary Inflammation and Emphysema: Role of the Cytokines IL-18 and IL-13.** *Am J Respir Crit Care Med* 2007, **176(1)**:49-62.
6. Nicolls MR, Taraseviciene-Stewart L, Rai PR, Badesch DB, Voelkel NF: **Autoimmunity and pulmonary hypertension: a perspective.** *Eur Respir J* 2005, **26(6)**:1110-1118.
7. Taraseviciene-Stewart L, Nicolls MR, Kraskauskas D, Scerbavicius R, Burns N, Cool C, Wood K, Parr JE, Boackle SA, Voelkel NF: **Absence of T cells confers increased pulmonary arterial hypertension and vascular remodeling.** *Am J Respir Crit Care Med* 2007, **175(12)**:1280-1289.
8. Lenschow DJ, Walunas TL, Bluestone JA: **CD28/B7 system of T cell costimulation.** *Annu Rev Immunol* 1996, **14**:233-258.
9. Croft M: **Co-stimulatory members of the TNFR family: keys to effective T-cell immunity?** *Nat Rev Immunol* 2003, **3(8)**:609-620.
10. Sugamura K, Ishii N, Weinberg AD: **Therapeutic targeting of the effector T-cell co-stimulatory molecule OX40.** *Nat Rev Immunol* 2004, **4(6)**:420-431.
11. Mestas J, Crampton SP, Hori T, Hughes CC: **Endothelial cell co-stimulation through OX40 augments and prolongs T cell cytokine synthesis by stabilization of cytokine mRNA.** *Int Immunol* 2005, **17(6)**:737-747.
12. Kotani A, Hori T, Matsumura Y, Uchiyama T: **Signaling of gp34 (OX40 ligand) induces vascular endothelial cells to produce a CC chemokine RANTES/CCL5.** *Immunol Lett* 2002, **84(1)**:1-7.
13. Gramaglia I, Weinberg AD, Lemon M, Croft M: **Ox-40 ligand: a potent costimulatory molecule for sustaining primary CD4 T cell responses.** *J Immunol* 1998, **161(12)**:6510-6517.
14. Murata K, Ishii N, Takano H, Miura S, Ndhlovu LC, Nose M, Noda T, Sugamura K: **Impairment of antigen-presenting cell function in mice lacking expression of OX40 ligand.** *J Exp Med* 2000, **191(2)**:365-374.
15. Rogers PR, Song J, Gramaglia I, Killeen N, Croft M: **OX40 promotes Bcl-xL and Bcl-2 expression and is essential for long-term survival of CD4 T cells.** *Immunity* 2001, **15(3)**:445-455.
16. Soroosh P, Ine S, Sugamura K, Ishii N: **OX40-OX40 ligand interaction through T cell-T cell contact contributes to CD4 T cell longevity.** *J Immunol* 2006, **176(10)**:5975-5987.
17. Soroosh P, Ine S, Sugamura K, Ishii N: **Differential Requirements for OX40 Signals on Generation of Effector and Central Memory CD4+ T Cells.** *J Immunol* 2007, **179(8)**:5014-5023.
18. Maxwell JR, Weinberg A, Prell RA, Vella AT: **Danger and OX40 receptor signaling synergize to enhance memory T cell survival by inhibiting peripheral deletion.** *J Immunol* 2000, **164(1)**:107-112.
19. Murata K, Nose M, Ndhlovu LC, Sato T, Sugamura K, Ishii N: **Constitutive OX40/OX40 ligand interaction induces autoimmune-like diseases.** *J Immunol* 2002, **169(8)**:4628-4636.
20. Satoh K, Kagaya Y, Nakano M, Ito Y, Ohta J, Tada H, Karibe A, Minegishi N, Suzuki N, Yamamoto M, *et al*: **Important role of endogenous erythropoietin system in recruitment of endothelial progenitor cells in hypoxia-induced pulmonary hypertension in mice.** *Circulation* 2006, **113(11)**:1442-1450.
21. Marzo AL, Vezys V, Williams K, Tough DF, Lefrancois L: **Tissue-level regulation of Th1 and Th2 primary and memory CD4 T cells in response to Listeria infection.** *J Immunol* 2002, **168(9)**:4504-4510.
22. Lander E, Kruglyak L: **Genetic dissection of complex traits: guidelines for interpreting and reporting linkage results.** *Nat Genet* 1995, **11(3)**:241-247.
23. Morris JA, Gardner MJ: **Calculating confidence intervals for relative risks (odds ratios) and standardised ratios and rates.** *Br Med J (Clin Res Ed)* 1988, **296(6632)**:1313-1316.
24. Sakaguchi S: **Naturally arising CD4+ regulatory t cells for immunologic self-tolerance and negative control of immune responses.** *Annu Rev Immunol* 2004, **22**:531-562.
25. Hadeiba H, Locksley RM: **Lung CD25 CD4 regulatory T cells suppress type 2 immune responses but not bronchial hyperreactivity.** *J Immunol* 2003, **170(11)**:5502-5510.

26. Lewkowich IP, Herman NS, Schleifer KW, Dance MP, Chen BL, Dienger KM, Sproles AA, Shah JS, Kohl J, Belkaid Y, *et al*: **CD4+CD25+ T cells protect against experimentally induced asthma and alter pulmonary dendritic cell phenotype and function.** *J Exp Med* 2005, **202(11)**:1549-1561.
27. McKinley L, Logar AJ, McAllister F, Zheng M, Steele C, Kolls JK: **Regulatory T cells dampen pulmonary inflammation and lung injury in an animal model of pneumocystis pneumonia.** *J Immunol* 2006, **177(9)**:6215-6226.
28. Bodolay E, Csipo I, Gal I, Sipka S, Gyimesi E, Szekanecz Z, Szegedi G: **Anti-endothelial cell antibodies in mixed connective tissue disease: frequency and association with clinical symptoms.** *Clin Exp Rheumatol* 2004, **22(4)**:409-415.
29. Vegh J, Szodoray P, Kappelmayer J, Csipo I, Udvardy M, Lakos G, Aleksza M, Soltesz P, Szilagyi A, Zeher M, *et al*: **Clinical and immunoserological characteristics of mixed connective tissue disease associated with pulmonary arterial hypertension.** *Scand J Immunol* 2006, **64(1)**:69-76.
30. Wang X, Ria M, Kelmenson PM, Eriksson P, Higgins DC, Samnegard A, Petros C, Rollins J, Bennet AM, Wiman B, *et al*: **Positional identification of TNFSF4, encoding OX40 ligand, as a gene that influences atherosclerosis susceptibility.** *Nat Genet* 2005, **37(4)**:365-372.
31. van Wanrooij EJ, van Puijvelde GH, de Vos P, Yagita H, van Berkel TJ, Kuiper J: **Interruption of the Tnfrsf4/Tnfsf4 (OX40/OX40L) pathway attenuates atherogenesis in low-density lipoprotein receptor-deficient mice.** *Arterioscler Thromb Vasc Biol* 2007, **27(1)**:204-210.
32. Takeda I, Ine S, Killeen N, Ndhlovu LC, Murata K, Satomi S, Sugamura K, Ishii N: **Distinct roles for the OX40-OX40 ligand interaction in regulatory and nonregulatory T cells.** *J Immunol* 2004, **172(6)**:3580-3589.
33. Ohshima Y, Yang LP, Uchiyama T, Tanaka Y, Baum P, Sergerie M, Hermann P, Delespesse G: **OX40 costimulation enhances interleukin-4 (IL-4) expression at priming and promotes the differentiation of naive human CD4(+) T cells into high IL-4-producing effectors.** *Blood* 1998, **92(9)**:3338-3345.
34. Hoshino A, Tanaka Y, Akiba H, Asakura Y, Mita Y, Sakurai T, Takaoka A, Nakaike S, Ishii N, Sugamura K, *et al*: **Critical role for OX40 ligand in the development of pathogenic Th2 cells in a murine model of asthma.** *Eur J Immunol* 2003, **33(4)**:861-869.
35. Nakae S, Saijo S, Horai R, Sudo K, Mori S, Iwakura Y: **IL-17 production from activated T cells is required for the spontaneous development of destructive arthritis in mice deficient in IL-1 receptor antagonist.** *Proc Natl Acad Sci USA* 2003, **100(10)**:5986-5990.
36. Kotake S, Udagawa N, Takahashi N, Matsuzaki K, Itoh K, Ishiyama S, Saito S, Inoue K, Kamatani N, Gillespie MT, *et al*: **IL-17 in synovial fluids from patients with rheumatoid arthritis is a potent stimulator of osteoclastogenesis.** *J Clin Invest* 1999, **103(9)**:1345-1352.
37. Fujino S, Andoh A, Bamba S, Ogawa A, Hata K, Araki Y, Bamba T, Fujiyama Y: **Increased expression of interleukin 17 in inflammatory bowel disease.** *Gut* 2003, **52(1)**:65-70.
38. Zhu Z, Ma B, Zheng T, Homer RJ, Lee CG, Charo IF, Noble P, Elias JA: **IL-13-induced chemokine responses in the lung: role of CCR2 in the pathogenesis of IL-13-induced inflammation and remodeling.** *J Immunol* 2002, **168(6)**:2953-2962.
39. Daley E, Emson C, Guignabert C, de Waal Malefyt R, Louten J, Kurup VP, Hogaboam C, Taraseviciene-Stewart L, Voelkel NF, Rabinovitch M, *et al*: **Pulmonary arterial remodeling induced by a Th2 immune response.** *J Exp Med* 2008, **205(2)**:361-372.
40. Deng Z, Morse JH, Slager SL, Cuervo N, Moore KJ, Venetos G, Kalachikov S, Cayanis E, Fischer SG, Barst RJ, *et al*: **Familial primary pulmonary hypertension (gene PPH1) is caused by mutations in the bone morphogenetic protein receptor-II gene.** *Am J Hum Genet* 2000, **67(3)**:737-744.
41. Morse JH, Deng Z, Knowles JA: **Genetic aspects of pulmonary arterial hypertension.** *Ann Med* 2001, **33(9)**:596-603.
42. Quinlan TR, Li D, Laubach VE, Shesely EG, Zhou N, Johns RA: **eNOS-deficient mice show reduced pulmonary vascular proliferation and remodeling to chronic hypoxia.** *Am J Physiol Lung Cell Mol Physiol* 2000, **279(4)**:L641-650.
43. Steudel W, Scherrer-Crosbie M, Bloch KD, Weimann J, Huang PL, Jones RC, Picard MH, Zapol WM: **Sustained pulmonary hypertension and right ventricular hypertrophy after chronic hypoxia in mice with congenital deficiency of nitric oxide synthase 3.** *J Clin Invest* 1998, **101(11)**:2468-2477.
44. Droma Y, Hanaoka M, Ota M, Katsuyama Y, Koizumi T, Fujimoto K, Kobayashi T, Kubo K: **Positive association of the endothelial nitric oxide synthase gene polymorphisms with high-altitude pulmonary edema.** *Circulation* 2002, **106(7)**:826-830.
45. Ono M, Sawa Y, Mizuno S, Fukushima N, Ichikawa H, Bessho K, Nakamura T, Matsuda H: **Hepatocyte growth factor suppresses vascular medial hyperplasia and matrix accumulation in advanced pulmonary hypertension of rats.** *Circulation* 2004, **110(18)**:2896-2902.
46. Ito W, Kanehiro A, Matsumoto K, Hirano A, Ono K, Maruyama H, Kataoka M, Nakamura T, Gelfand EW, Tanimoto M: **Hepatocyte growth factor attenuates airway hyperresponsiveness, inflammation, and remodeling.** *Am J Respir Cell Mol Biol* 2005, **32(4)**:268-280.
47. Niedbala W, Wei XQ, Campbell C, Thomson D, Komai-Koma M, Liew FY: **Nitric oxide preferentially induces type 1 T cell differentiation by selectively up-regulating IL-12 receptor beta 2 expression via cGMP.** *Proc Natl Acad Sci USA* 2002, **99(25)**:16186-16191.
48. Ivy DD, McMurtry IF, Colvin K, Imamura M, Oka M, Lee DS, Gebb S, Jones PL: **Development of occlusive neointimal lesions in distal pulmonary arteries of endothelin B receptor-deficient rats: a new model of severe pulmonary arterial hypertension.** *Circulation* 2005, **111(22)**:2988-2996.

**doi:10.1186/1471-2172-12-67**
**Cite this article as:** Rabieyousefi *et al.*: Indispensable roles of OX40L-derived signal and epistatic genetic effect in immune-mediated pathogenesis of spontaneous pulmonary hypertension. *BMC Immunology* 2011 **12**:67.

Proceedings of the 5th International
IEEE EMBS Conference on Neural Engineering
Cancun, Mexico, April 27 - May 1, 2011



# Development of Si Neural Probe with Optical Waveguide for Highly Accurate Optical Stimulation of Neuron

R. Kobayashi, S. Kanno, S. Sakai, S. Lee, M. Koyanagi, H. Yao, and T. Tanaka

*Abstract*— **Lots of researchers take great interests in brain science. In this area, measurement devices of the brain have been developed by number of groups, and played an important role. Recently, for neuroengineering applications such as optogenetics, optical stimulation devices which consisted of optical fibers have been reported, and used to deliver light to neurons expressing light sensitive channel proteins. However, accurate stimulation of neurons could not be achieved by using these devices because of optical fibers with a diameter of over 100 μm. Here, we have proposed a novel Si neural probe with micromachined optical waveguide for multiple and precise optical stimulations of neurons. SiN film was employed as the optical waveguide core due to its optical transmission characteristics. Both the light propagation in the optical waveguide and controllability of output patterns of the light were clearly confirmed by optical experiments using a blue laser. *In vitro* experiments of optical stimulation of neurons using the fabricated Si neural probe were performed. A CA1 area of a thin hippocampal slice obtained from the brain of a transgenic rat expressing Channelrhodopsin-2 (ChR2) was employed. We stimulated neurons optically using the Si neural probe and successfully observed increases of firing rates in neurons accordingly with the light exposure.**

## I. Introduction

RECENTLY various studies related with a brain such as medical treatments for brain diseases, analysis of brain functions, and brain-machine interface (BMI) have been strongly promoted. For researches, various kinds of neural probes have been developed to record neuronal action potentials and other brain activities. Especially, due to strong requirement of high density recording of neuronal activities for further minute brain analysis, various types of Si neural probes which enable high density recording have been developed [1]-[3]. We have also proposed an implantable intelligent Si neural probe system which has multifunctional property [4], [5]. We reported novel double-sided Si neural probes for *in vitro* and *in vivo* recording, and we successfully recorded neuronal action potentials from brains of a guinea pig and a macaque using the fabricated double-sided Si neural probes. The Si neural probe with a microfluidic channel has been also reported, and we demonstrated fluid delivery of the fabricated Si neural probe with a microfluidic channel.

In this paper, we proposed a novel Si neural probe with optical waveguide for optical stimulation of neurons. We determined a material of the optical waveguide carefully and fabricated a Si neural probe with optical waveguide. We assembled the fabricated Si neural probe with an optical fiber and evaluated optical characteristics such as a propagation pattern in the optical waveguide and output patterns of the light. Subsequently, we performed an *in vitro* experiment of optical stimulation of neurons in a hippocampal slice obtained from transgenic rat expressing ChR2 using the fabricated Si neural probe, and performed an extracellular recording of neuronal action potentials using a glass electrode.

R. Kobayashi, S. Kanno, S. Lee, T. Tanaka are with the Department of Biomedical Engineering, Graduate School of Biomedical Engineering, Tohoku University, 6-6-01 Aza-Aoba, Aramaki, Aoba-ku, Sendai 980-8579, Japan (corresponding author, phone: +81-22-795-6258; e-mail: link@lbc.mech.tohoku.ac.jp).

S. Sakai and H. Yao are with the Department of Biology and Neuroscience, Graduate School of Life Sciences, Tohoku University, 2-1-1 Katahira, Aoba-ku, Sendai 980-8577, Japan.

M. Koyanagi is with the New Industry Creation Hatchery Center, Tohoku University, 6-6-10 Aza-Aoba, Aramaki, Aoba-ku, Sendai 980-8579, Japan.

## II. Probe Fabrication and Characteristics

### A. Proposal of Si neural probe with optical waveguide

Direct optical stimulation of genetically targeted neurons expressing the light sensitive channel protein such as ChR2 has recently reported [6]. This offers the prospect of enabling local delivery of millisecond temporal controlled optical stimulation with cell-type selectivity. Various kinds of neural probes which have the capability of an optical stimulation have been reported [7]-[9]. Almost these neural probes ever developed were based on or consisted of an optical fiber which was used for an optical communication system. Comparing with conventional optical sources, including band-filtered white light, light emitting diodes (LED) or laser-coupled optics, this realized a local optical stimulation and an easy and low-cost fabrication process of the probes. However, an optical fiber generally has a diameter of over 100 μm, and these probes have only one stimulation site because of an optical fiber with a single core. Therefore, to realize multiple optical stimulations, neurophysiologists have to employ bundled optical fibers with a millimeter-sized diameter which causes large neuron damages. Additionally, for an accurate and simultaneous neuronal activities recording with an optical stimulation, stimulation sites should be placed on neural probes directly.

Hence, we proposed a novel Si neural probe with micromachined optical waveguide for optical stimulation of neurons. Since many optical waveguides of a few micrometers can be simultaneously fabricated on the Si neural probe, multiple and highly accurate optical stimulations can be realized. Furthermore, by using micromachining technology, the optical outlet field can be controlled purposefully. The optogenetic methodology would

978-1-4244-4141-9/11/$25.00 ©2011 IEEE

be dramatically improved by integrating optical waveguide with our double-sided recording and fluid delivery technology, as shown in Fig. 1. Here, to confirm the fundamental characteristics of optical waveguide, we fabricated the Si neural probe with an optical waveguide.

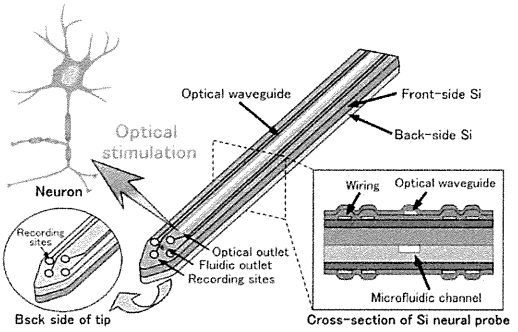


Fig. 1. Multifunctional Si neural probe with optical waveguide, microfluidic channel, and double-sided recording sites.

### *B. Fabrication of Si neural probe with optical waveguide*

The Si neural probe was fabricated by standard micromachining process. We employed SiN film as the optical waveguide core, because its optical transmission characteristics is appropriate to the excitation spectrum of ChR2 and SiN is one of the most conventional material used in micromachining process. Transmission characteristics of a 1.5-μm-thick SiN film are shown in Fig. 2. A sensitive waveband of a cell expressing ChR2 was 400–560 nm, and the sensitivity of the cell was maximal at wavelengths around approximately 480 nm [10]. As shown in the figure, SiN film has high transmittance in the sensitive waveband of the cell expressing ChR2.

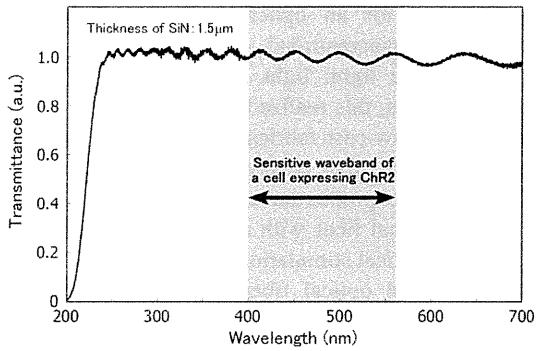


Fig. 2. Transmission characteristics of a 1.5-μm-thick SiN film.

The fabrication sequence of the Si probe is illustrated in Fig. 3. A 100-μm-thick Si wafer was used as the substrate of the probe. First, a 1.0-μm-thick $SiO_2$ layer was formed by thermal oxidation. Then, an 800-nm-thick SiN waveguide core was formed by plasma-enhanced chemical vapor deposition (PECVD) and reactive-ion etching (RIE) with $SF_6$ and $O_2$ gases. Next, a 500-nm-thick $SiO_2$ waveguide clad was formed by PECVD. Then, Au/Cr wirings were formed on the surface of the wafer by sputtering and wet etching with an iodine etchant and a ceric ammonium nitrate solution. The thicknesses of Au and Cr were 250 and 50 nm, respectively. Then, a 1.0-μm-thick $SiO_2$ layer was deposited by PECVD for insulation of the wirings. After that, both recording sites and bonding pads were formed by wet etching with buffered HF solution ($HF/NH_4F$:1/10), followed by formation of optical inlets by RIE. Finally, the probe shape was formed by deep reactive-ion etching (DRIE) with $SF_6$ and $C_4F_8$ gases. As a result, the Si neural probe with optical waveguide was obtained.

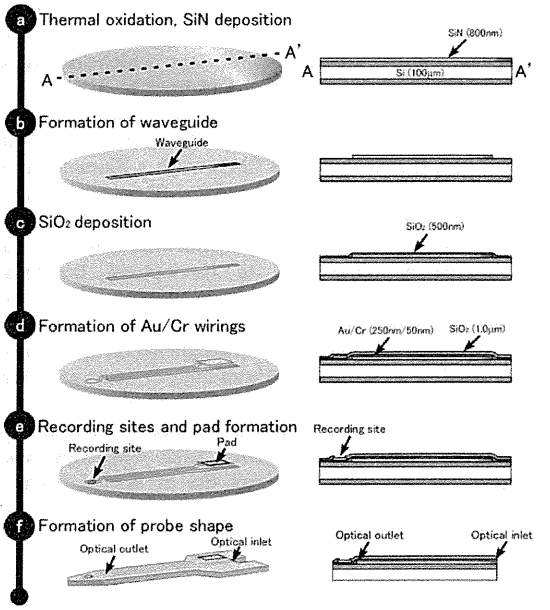


Fig. 3. Fabrication sequence of the Si neural probe with the optical waveguide.

Figure 4 shows photographs of the fabricated Si neural probe with the optical waveguide. This Si neural probe is 40-mm length for measuring deeper region of the brain. The width and thickness of the Si neural probe are 160 μm and 100 μm, respectively. An optical outlet used as an optical stimulation site was located at the tip of the probe.

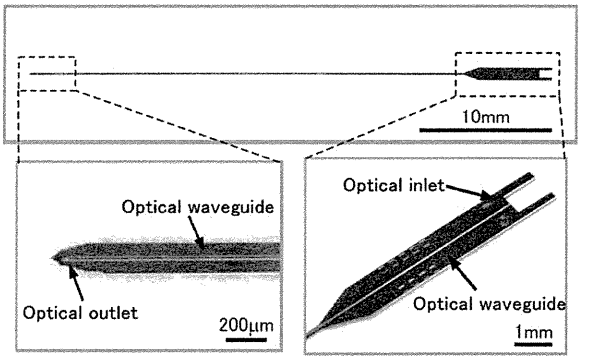


Fig. 4. Photographs of the fabricated Si neural probe with optical waveguide.

To evaluate the controllability of output patterns of the light, we prepared two types of outlet patterns such as 90-degrees angled pattern and 22.5-degrees angled pattern. At the end of the probe, an optical inlet part was formed to

connect with an optical fiber. Figure 5 shows SEM images of the probe tip with 22.5-degrees angled outlet pattern and the cross-section of the optical waveguide. As seen in the figure, the optical waveguide of SiN was well formed on the neural probe.

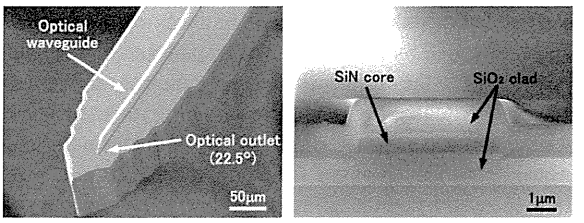


(a) Si neural probe tip (b) Cross-section of optical waveguide

Fig. 5. SEM images of the fabricated Si neural probe.

The precise alignment was required for connecting the Si neural probe to the optical fiber. Figure 6 shows the alignment procedure between the Si neural probe and the optical fiber. The optical fiber was successfully adjusted to the optical inlet position by tri-axial stage. The light leakage from the optical waveguide was measured as shown in Fig. 6 (b). After the alignment procedure, the optical fiber was connected using a UV-curable epoxy. An assembled system consisted of the Si neural probe with the optical waveguide, a glass epoxy board, and an optical fiber, as shown in Fig. 7.

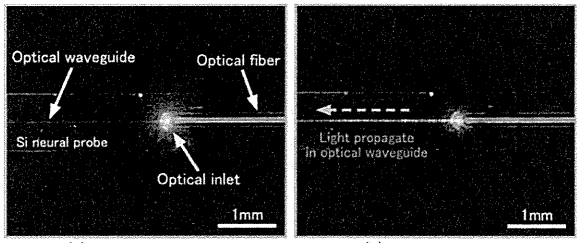


(a) Before alignment (b) After alignment

Fig. 6. Photographs of alignment procedure.

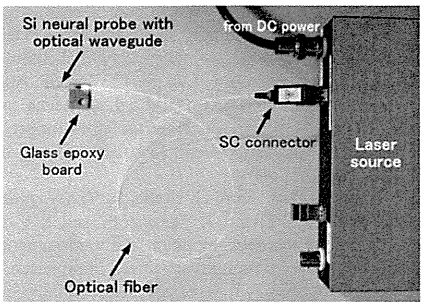


Fig. 7. Photograph of the fabricated Si neural probe assembly.

### C. *Evaluation of fabricated optical waveguide*

A cross-sectional near field pattern (NFP) of the 15-μm-width optical waveguide was measured by passing a blue laser with wavelength of 452 nm, as shown in Fig. 8. The multimode light propagation in the fabricated optical waveguide was clearly observed. Figure 9 shows the light output patterns from two types of the optical outlets with 5-μm-width optical waveguide. These images were taken in colloidal solution to observe the light output pathways by scattering. A difference of light output patterns between 90-degrees angled pattern and 22.5-degrees angled pattern were clearly observed. Especially, the light from 22.5-degrees angled pattern mainly turned 45-degrees direction by total reflection.

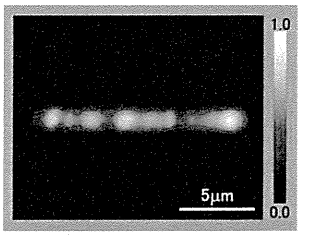


Fig. 8. Cross-sectional NFP of the fabricated optical waveguide.

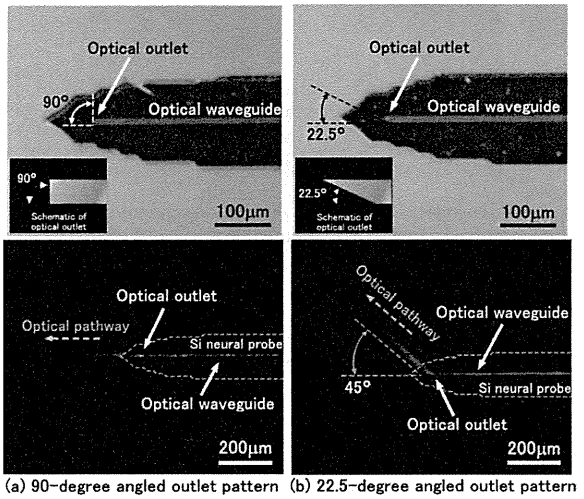


(a) 90-degree angled outlet pattern (b) 22.5-degree angled outlet pattern

Fig. 9. Photographs of the optical outlets and light output patterns.

## III. Animal Experiments using Fabricated Probe

We performed *in vitro* experiments of optical stimulation of neurons using the fabricated Si neural probe with optical waveguide, and we recorded neuronal action potentials using a glass electrode. All animal experiments were approved by the Tohoku University Committee for Animal Experiments and were carried out in accordance with the Guidelines for Animal Experiment and Related Activities in Tohoku University as well as the guiding principles of the Physiological Society of Japan and the NIH. The experiments were carried out using 28–35-day-old Thy1.2-ChR2-Venus rats. We followed the protocol previously described by Feng *et al.* [11] to generate Thy-1.2 transgenic rats. Neuronal action potentials were recorded from 400-μm-thick hippocampal slices obtained from the brains of Thy1.2-ChR2-Venus rats. The slices were kept in normal artificial cerebrospinal fluid (ACSF) containing (in mM) 120 NaCl, 2.5 KCl, 26 $NaHCO_3$, 1 $NaH_2PO_4$, 2.5 $CaCl_2$, 1.3 $MgCl_2$, 11 glucose, which was equilibrated with a gas mixture of 5 % $CO_2$ in $O_2$. The hippocampal slice was placed on a perfusing fluid chamber maintained at 35 ± 1 °C. Recordings

were made with an Axopatch200B amplifier (Axon Instruments, Foster City, CA) and amplified and filtered at 1 kHz with an FLA-01 amplifier (Cygnus Technology, Inc., Delaware Water Gap, PA), digitized at 10 kHz with a DigiDate 1400 A/D converter (Axon Instruments). Data were analyzed with Clampfit 10 software (Axon Instruments). The signals were filtered at 140 Hz again on the software. Neuronal action potentials were recorded extracellularly in the pyramidal cell layer of the CA1 area of the hippocampus using a glass electrode with a pipette resistance of 2 MΩ filled with 1.78 % $Na_2SO_4$ solution. The external laser source was connected to the fabricated Si neural probe assembly.

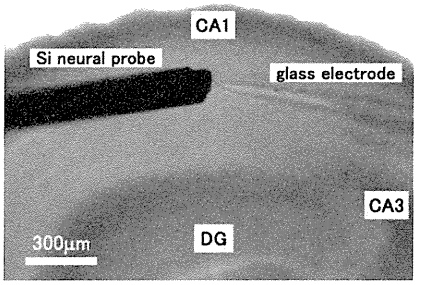


Fig. 10. Photograph of the Si probe with optical waveguide and a glass electrode inserted into the CA1 area of the hippocampal slice.

Figure 10 shows a photograph of the Si neural probe and a glass electrode inserted into the CA1 area of the hippocampal slice. The Si neural probe was preliminarily placed near the glass electrode using manipulators. The 490-nm-wavelength laser diode (LD) light was exposed from the outlet of the Si probe for 1 s. The power of the light exposed to neurons was estimated at 70–180 μW/mm$^2$.

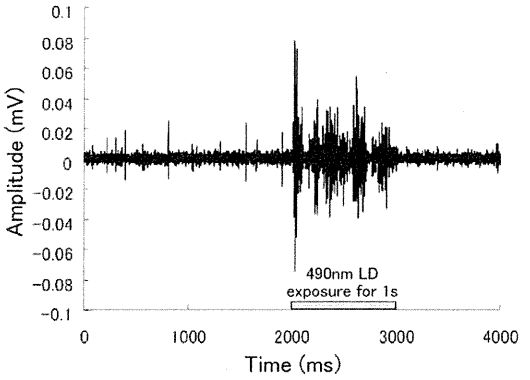


Fig. 11. Recorded neuronal action potentials induced by an optical stimulation using the fabricated Si neural probe with optical waveguide.

As shown in Fig. 11, we successfully recorded neuronal action potentials of multiple neurons. As shown in this figure, firing rate of neurons increased in accordance with the light exposure. It indicated that we successfully stimulated neurons optically using the fabricated Si neural probe with optical waveguide. The observed firing rate of neurons was not constant due to desensitization of ChR2 and activities of inhibitory neurons expressing ChR2.

## IV. Conclusion

We proposed the novel Si neural probe with optical waveguide for multiple optical stimulations of neurons. The SiN film was employed as the optical waveguide. The light propagation in the optical waveguide was confirmed by the NFP. The controllability of output patterns of the light was clearly confirmed by two outlet design patterns. It means that we can control the arbitrarily output patterns of the light. Using the fabricated Si neural probe, we performed *in vitro* experiments of optical stimulation of neurons in the hippocampal slice obtained from Thy1.2-ChR2-Venus rats. We successfully stimulated neurons optically and observed increases of neurons firing rates in accordance with the light exposure, indicating that we successfully stimulated neurons optically using the fabricated Si neural probe with optical waveguide.

## References


[1] A. M. Sodagar, K. D. Wise, and K. Najafi, "A Wireless Implantable Microsystem for Multichannel Neural Recording," *IEEE Trans. Microwave Theory and Techniques*, vol. 57, pp. 2565–2573, October 2009.

[2] J. Du1, M. L. Roukes, and S. C. Masmanidis, "Dual-side and three-dimensional microelectrode arrays fabricated from ultra-thin silicon substrates," *J. Micromech. Microeng.*, vol. 19, 075008, pp. 1–7, June 2009.

[3] T. Harimoto, K. Takei, T. Kawano, A. Ishihara, T. Kawashimac, H. Kanekod, M. Ishida, and S. Usui, "Enlarged gold-tipped silicon microprobe arrays and signal compensation for multi-site electroretinogram recordings in the isolated carp retina," *Biosensors and Bioelectronics*, to be published.

[4] R. Kobayashi, S. Kanno, S. Lee, J. Bea, T. Fukushima, K. Sakamoto, N. Katayama, H. Mushiake, T. Tanaka, and M. Koyanagi, "Development of Si Double-Sided Microelectrode for Platform of Brain Signal Processing System," *Jap. J. Appl. Phys.*, vol. 48, 04C194, pp. 1–5, April 2009.

[5] S. Kanno, R. Kobayashi, S. Lee, J. Bea, T. Fukushima, K. Sakamoto, N. Katayama, H. Mushiake, T. Tanaka, and M. Koyanagi, "Development of Si Neural Probe with Microfluidic Channel Fabricated Using Wafer Direct Bonding," *Jap. J. Appl. Phys.*, vol. 48, 04C189, pp. 1–4, April 2009.

[6] E. S. Boyden, F. Zhang, E. Bamberg, G. Nagel, and K. Deisseroth, "Millisecond-timescale, genetically targeted optical control of neural activity," *Nature Neuroscience*, vol. 8, pp. 1263–1268, August 2005.

[7] F. Zhang, A. M. Aravanis, A. Adamantidis, L. de Lecea, and K. Deisseroth, "Circuit-breakers: optical technologies for probing neural signals and systems," *Nature Reviews Neuroscience*, vol. 8, pp. 577–581, August 2007.

[8] J. Zhang, F. Laiwalla, J. A. Kim, H. Urabe, R. VanWagenen, Y. K. Song, B. W. Connors, F. Zhang, K. Deisseroth, and A. V. Nurmikko, "Integrated device for optical stimulation and spatiotemporal electrical recording of neural activity in light-sensitized brain tissue," *J. Neural Eng.*, vol. 6, 055007, pp. 1–13, September2009.

[9] S. Royer, B. V. Zemelman, M. Barbic, A. Losonczy, G. Buzsáki, J. C. Magee, "Multi-array silicon probes with integrated optical fibers: light-assisted perturbation and recording of local neural circuits in the behaving animal," *European Journal of Neuroscience*, vol. 31, pp. 2279–2291, March 2010.

[10] H. Wang, Y. Sugiyama, T. Hikima, E. Sugano, H. Tomita, T. Takahashi, T. Ishizuka, and H. Yawo, "Molecular Determinants Differentiating Photocurrent Properties of Two Channelrhodopsins from Chlamydomonas," *Journal of Biological Chemistry*, vol. 284, no. 9, pp. 5685–5696, February 2009.

[11] G. Feng, R. H. Mellor, M. Bernstein, C. KePeck, Q. T. Nguyen, M. Wallace, J. M. Nerbonne, J. W. Lichtman, and J. R. Sanes, "Imaging neuronal subsets in transgenic mice expressing multiple spectral variants of GFP," *Neuron*, vol. 28, pp. 41–51, October 2000.